FLASH SINTERING OF BISMUTH FERRITE IN-SITU USING ENERGY DISPERSIVE X-RAY DIFFRACTION

By

MARY ANNE WASSEL

A dissertation submitted to the

School of Graduate Studies

Rutgers, The State University of New Jersey

In partial fulfillment of the requirements

For the degree of

Doctor of Philosophy

Graduate Program in Materials Science and Engineering

Written under the direction of

Professor Thomas Tsakalakos

And approved by

_____

_____

_____

_____

New Brunswick, New Jersey

October 2018

ABSTRACT OF THE DISSERTATION

Flash Sintering of Bismuth Ferrite in-situ Using Energy Dispersive X-Ray Diffraction

by MARY ANNE WASSEL

Dissertation Director:

Professor Thomas Tsakalakos

Bismuth ferrite ($BiFeO_3$, or BFO) is a multiferroic oxide ceramic that has unique properties at the nanoscale level at room temperature. For this reason, it is of great interest to study and implement BFO's properties for use in a variety of applications, including multiferroic memory, spintronics, and photovoltaics. However, BFO is difficult to make in bulk, not only because impurity phases can develop and inhibit its multiferroic properties, but also because the phase transition at 825°C from its ferroelectric to paraelectric state acts against the densification process.

Flash sintering is a relatively new densification technique that takes less time and energy to make bulk ceramics while exposing the sample to a low electric field. In this study, we investigate the feasibility of flash sintering bismuth ferrite at temperatures below 825°C. Densification occurred at furnace temperatures of 500°C and 350°C, much lower than the transition temperature, to approximately 90% of the theoretical density. During this process, it was observed via energy dispersive X-ray diffraction, a rapid characterization technique used to probe crystallography of bulk materials, that anisotropic lattice expansion occurs when BFO is exposed to an electric field, which is not seen in conventional sintering. Estimating sample temperature during flash sintering is a difficult

process, and a few methods are discussed. Finally, several theoretical models of flash sintering mechanisms are addressed to aid in understanding of how this technique works.

ACKNOWLEDGEMENT

I would like to thank my adviser, Dr. Thomas Tsakalakos, for his support, feedback, and trust in me throughout my project. Thanks also to my thesis committee for their participation: Dr. Lisa Klein, Dr. Adrian Mann, and Dr. Luis Pérez-Maqueda. I am additionally grateful to Dr. Pérez-Maqueda and his team, including Eva Gil-González and Antonio Perejón, at the Instituto de Ciencia de Materiales de Sevilla and the Universidad de Sevilla for providing the bismuth ferrite and their useful collaboration and feedback. This research used resources of the Advanced Photon Source, a U.S. Department of Energy (DOE) Office of Science User Facility operated for the DOE Office of Science by Argonne National Laboratory under Contract No. DE-AC02-06CH11357. I very much appreciate the support that Dr. John Okasinski provided during experiments at APS at 6-BM-A. Thanks to Antti Makinen of the Office of Naval Research for feedback and interest in our lab's work. The Office of Naval Research generously funded my studies via contracts N00014-15-1-2492-438700 and 4104-78982-820133.

Thank you to the Nanomaterials Laboratory group members for assistance in my work, especially: Shikhar Jha, Harry Charalambous, Avaniek Cabales, Dennis Trofimchuk Michael Foderaro, Ruben Papraniku, Ryan Lay, Kent Christian, Hulya Bicer, Tevfik Ozdemir, and Will Paxton.

Many thanks to my Rutgers colleagues over the years for their support and friendship, particularly: Terence Whalen, Brian Viezbicke, Lara Baroudi, Berra Beyoglu, Josh Epstein, Rut Rivera, Ilya Chigirev, Will Schneekloth, Elaheh Taghaddos, Mark Schafer, Mustafa Alazzawi, Elliott Dolan, Will Hansen, and Melody Wren. Thanks to members of the SWE Grad Board who kept me going: Ashley Pennington, Alessia Eramo,

Alison Acevedo, Tahsina Farah Sanam, Adriana Trias, and Parneet Kaur. Thanks additionally to those whose wisdom and expertise encouraged me along the way, including Jared Camins, Shari Perkins, Dr. Ron Graham, Keri Flanagan, Ed Osoliniec, Dr. George Bennett, Dr. Mark Forest, Dr. Sarah Meyer, and Michael Lepak.

Lastly, but most importantly, I owe so much to my family who supported my decision to pursue my academic career. My path has not been an easy or straightforward one, and I couldn't have done it without you all. And Bryan, words can't describe how important you have been in this process and in my life. There is no one I'd rather have by my side. You are my rock!

TABLE OF CONTENTS

LIST OF TABLES

LIST OF FIGURES

1. INTRODUCTION

Bismuth ferrite ($BiFeO_3$, or BFO) is a multiferroic oxide ceramic that has unique properties at the nanoscale level at room temperature. For this reason, it is of great interest to study and exploit BFO's properties for use in a variety of applications, including multiferroic memory, spintronics, and photovoltaics.

That said, pure BFO is very difficult to fabricate as it is considered metastable, arguably even at room temperature. Impurity phases, namely $Bi_{23}FeO_{39}$ and $Bi_2Fe_4O_9$, can arise both when creating the powder and during sintering that adversely affect the material properties. It was recently found that forming bulk BFO with improved properties can be facilitated by starting with nanoparticles processed mechanochemically.

An additional challenge in sintering BFO is that the phase transitions from antiferromagnetic to ferroelectric and from ferroelectric to paraelectric involve changes in the crystal lattice that work against the densification process.

Electric field assisted sintering techniques (FAST) have been implemented in ceramic manufacturing to reduce the sintering time and temperature. Flash sintering is recently discovered technique that sinters ceramics in seconds at temperatures much lower than conventional sintering requires. Furthermore, flash sintering requires no applied pressure to the sample during the densification process.

Through a collaboration with the Pérez-Maqueda Reactivity of Solids group at the Instituto de Ciencia de Materiales de Sevilla, it is of mutual interest to fabricate pure BFO in bulk efficiently. The aim of this thesis is to use energy-dispersive X-ray diffraction (EDXRD) in-situ to study the sintering mechanisms and behavior of flash sintering

nanostructured bismuth ferrite. EDXRD is a rapid and useful tool for extracting information about material phase makeup and changes in bulk materials.

Through this work, ideal flash conditions for BFO will be developed and the resulting material properties will be compared to those of conventional sintering methods. There will be evidence and discussion of flash sintering below BFO's paraelectric phase transition and how the lattice responds to electric field exposure. There will also be some discussion about how to effectively estimate the sample temperature during flash sintering. Because flash sintering is such a new technique, it is unclear what the mechanisms are for such rapid densification, especially because they tend to vary depending on the material being densified. Unification of several mechanism models is proposed to explain flash sintering of bismuth ferrite.

2. LITERATURE REVIEW

2.1. Bismuth Ferrite

Bismuth ferrite ($BiFeO_3$, or BFO) is a rhombohedrally-distorted perovskite-type ferrite material and one of the few multiferroic oxide materials that has both antiferromagnetic and ferroelectric phases that exist above room temperature[1, 2]. BFO was found to have an antiferromagnetic G-type spin configuration[2].

2.1.1. Crystal Structure and Phase Diagram

Bismuth ferrite has a rhombohedral structure at room temperature and belongs to the R3c space group. Due to the mismatched ion sizes, the oxygen octahedra in BFO have to buckle to squeeze into the unit cell[3]. This structural parameter is quantified by the Goldschmid tolerance factor[3], which for BFO is 0.88. Consequently, the Fe-O-Fe angle $\theta \approx 154° - 156°$, determines the magnetic ordering and conductivity of the material[3]. Fischer et al[4] found that the tilt angle of the oxygen octahedral decreases almost linearly from 12.5° at -269°C to 11.4° at 605°C.

The crystal geometry equation and unit cell volume equation for a rhombohedral structure in terms of the interplanar spacing and values of (hkl) are shown in Equations (1) and (2):

$$\frac{1}{d^2} = \frac{(h^2 + k^2 + l^2)\sin^2\alpha_{\text{rhom}} + 2(hk + kl + hl)(\cos^2\alpha_{\text{rhom}} - \cos\alpha_{\text{rhom}})}{a_{\text{rhom}}^2(1 - 3\cos^2\alpha_{\text{rhom}} + 2\cos^3\alpha_{\text{rhom}})} \quad (1)$$

$$V = a_{\text{rhom}}^3\sqrt{1 - 3\cos^2\alpha_{\text{rhom}} + 2\cos^3\alpha_{\text{rhom}}} \quad (2)$$

A rhombohedral unit cell can be approximated with a hexagonal structure (see Figure 1[5]).

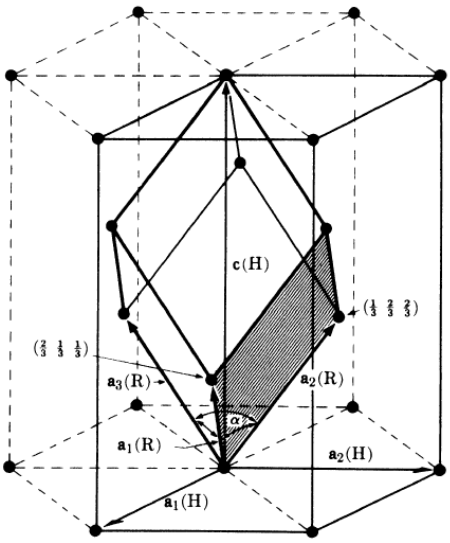

Figure 1: Relation between rhombohedral and hexagonal crystal structure

The crystal geometry equation and unit cell volume equation for a hexagonal structure are shown in Equations (3) and (4):

$$\frac{1}{d^2} = \frac{4}{3}\left(\frac{h^2 + hk + k^2}{a_{\text{hex}}^2}\right) + \frac{l^2}{c_{\text{hex}}^2} \quad (3)$$

$$V = \frac{\sqrt{3}a_{\text{hex}}^2 c_{\text{hex}}}{2} \quad (4)$$

It is much easier to determine the hexagonal lattice parameters, so it is often useful to find the rhombohedral lattice parameters in terms of them. Their relations are shown in Equations (5) and (6):

$$a_{\text{rhom}} = \frac{1}{3}\sqrt{3a_{\text{hex}}^2 + c_{\text{hex}}^2} \quad (5)$$

$$\alpha_{\text{rhom}} = 2\sin^{-1}\left(\frac{3}{2\sqrt{3 + (c_{\text{hex}}/a_{\text{hex}})^2}}\right) \quad (6)$$

The crystal structure bismuth ferrite is shown in Figure 2[6]:

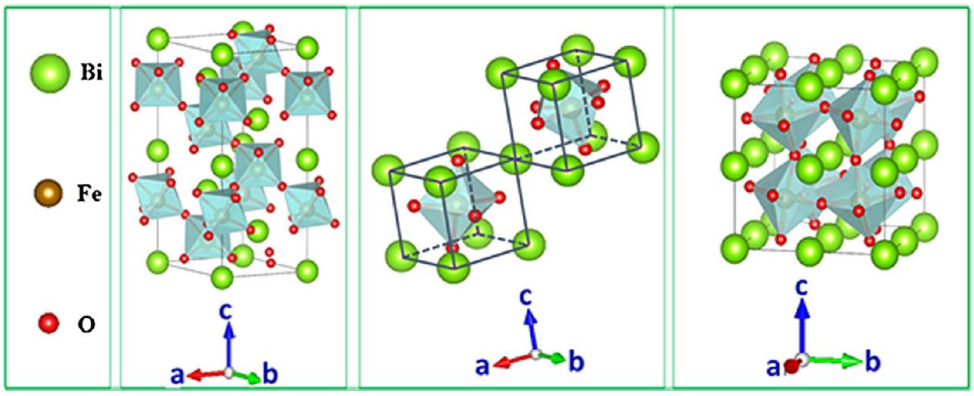

(a) (b) (c)

Figure 2: Crystal structure of BFO, where (a) shows a hexagonal unit cell, (b) shows two pseudocubic cells along [111], (c) shows a 2×2×2 super cell

Michel et al employed a double cell to account for an observed superstructure[7]. Kubel et al[8] found the following lattice parameters by experiment, which are consistent with data from literature[4, 7] and shown in Table 1.

Table 1: Measured hexagonal and rhombohedral lattice parameters

$a_{\text{hex}} = 5.57874$ Å $c_{\text{hex}} = 13.8688$ Å	$a_{\text{rhom}} = 5.6343$ Å $\alpha_{\text{rhom}} = 59.348°$

A phase diagram of bismuth ferrite is shown in Figure 4[9]. Bismuth ferrite has a Néel temperature in the range of 350-370°C [10] at which point it transitions from antiferromagnetic to paramagnetic. This antiferromagnetism is shown in Figure 3[6]:

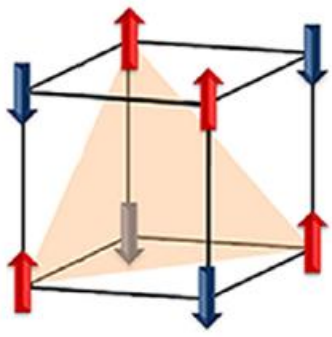

Figure 3: Schematic of G-type antiferromagnetic ordering below the Néel temperature

The Curie temperature is in the range of 810-830°C [10], at which point the crystal structure undergoes a reversible phase transformation from rhombohedral to orthorhombic. The rhombohedral phase is maintained through 605°C, at which point the octahedral tilt begins to slowly change[10]. A cubic phase is attained at temperatures above 920°C [10].

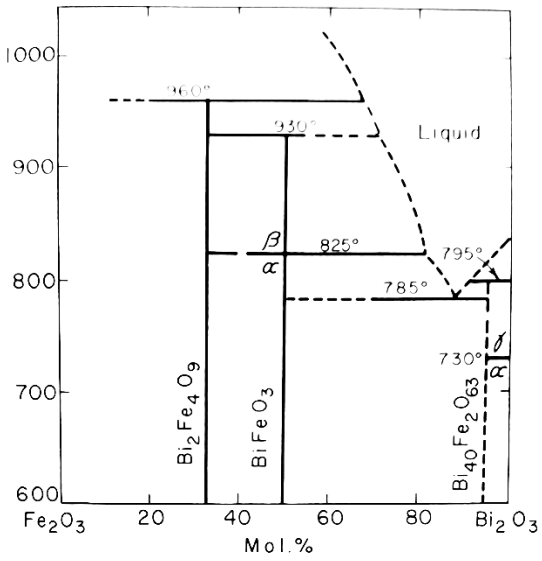

Figure 4: Phase diagram of BFO

No phase diagrams exist for bismuth ferrite below 600°C.

2.1.2. Physical Properties

2.1.2.1. Density

The theoretical density of bismuth ferrite is 8.2 g/cm^3 at room temperature.

2.1.2.2. Thermal Expansion Coefficient

The thermal expansion coefficients based on hexagonal lattice parameters and temperature were first determined by Bucci et al[7] and are shown in Table 2 and Figure 5:

Table 2: Hexagonal Lattice Parameters and Thermal Expansion Coefficients for BFO Based on Temperature

Temperature Range, T (℃)	**Hexagonal Lattice Parameters (Å)**	**Thermal Expansion Coefficients ($1/$℃)**
25.13-325	$a = 5.5764 + 6.06 \times 10^{-5}T$	$\alpha_a = 10.9 \times 10^{-6}$
	$c = 13.8620 + 2.10 \times 10^{-4}T$	$\alpha_c = 15.1 \times 10^{-6}$
344-838	$a = 5.5946 + 6.83 \times 10^{-5}T$	$\alpha_a = 12.2 \times 10^{-6}$
	$c = 13.7251 + 9.05 \times 10^{-4}T$ $-12.50 \times 10^{-7}T^2 + 9.40 \times$ $10^{-10}T^3 - 3.57 \times 10^{-13}T^4$	$\alpha_c = 65.0 \times 10^{-6} - 18.0 \times$ $10^{-8}T + 20.3 \times 10^{-11}T^2 -$ $10.3 \times 10^{-14}T^3$

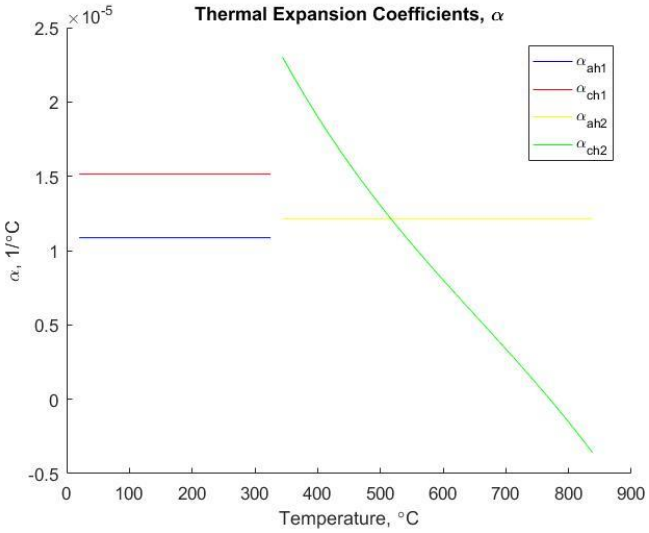

Figure 5: Temperature-Dependent Thermal Expansion Coefficients for BFO Based on Hexagonal Lattice Parameters

The break in temperature range is on account of the Néel temperature. The thermal expansion coefficient for the hexagonal lattice parameter a remains constant, but the thermal expansion coefficient for hexagonal lattice parameter c is a third order polynomial with a slope that concaves down.

Perejón et al[11] found that the thermal stability of BFO is not influenced by heating environment.

2.1.2.3. Thermodynamic Properties

Figure 6[12] details the relationship between specific heat and temperature. The specific heat exhibits a peak at the Néel temperature[12, 13]. The roto-antiferromagnetic coupling, χ, leads to a broadening in the specific heat jump.

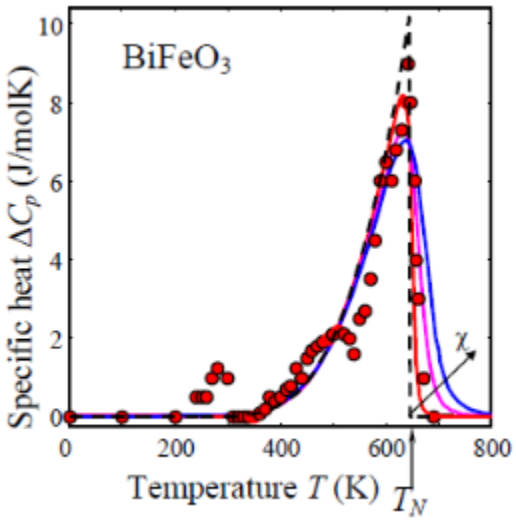

Figure 6: Temperature dependence of the specific heat of BFO

2.1.2.4. Electrical and Magnetic Properties

Bismuth ferrite is a multiferroic material. Its ferroelectricity comes from the active lone-pair orbital of bismuth ions which generate spontaneous polarization along the [111] axis of the rhombohedral unit cell since these ions are displaced with respect to the FeO_6 octahedra[14].

Rojac et al[15] investigated the piezoelectric effect at elevated temperatures and found that the strong temperature dependence is from BFO's local electrical conductivity.

Selected electrical properties of BFO are shown in Table 3. BFO is subject to large leakage currents and low electrical resistivity due to oxygen vacancies, secondary phases,

and iron ions with different valences induced by bismuth volatilization[16]. It is consequently difficult to synthesize, and to get good polarization hysteresis and remanent polarization.

Table 3: Selected Electrical Properties of BFO

Property	Value
Coercivity	115 Oe [17]
Resistivity	$> 10^{10}\ \Omega \cdot \mathrm{cm}$ [18]
Conductivity	$\ll 10^{7} \Omega^{-1} \cdot \mathrm{cm}^{-1}$ [18]
Dielectric constant	30 [3], 129-685 [19]
Piezoelectric coefficient	$15 - 60\ \mathrm{pv\ V}^{-1}$ [3]
Band gap	1.3 eV [20]
Activation energy for conduction	1.15 eV [18]
Remanent polarization along [111]	$100\ \mu\mathrm{C\ cm}^{-1}$ [3]

The polarization hysteresis for sintered BFO at several temperatures is shown in Figure 7[21].

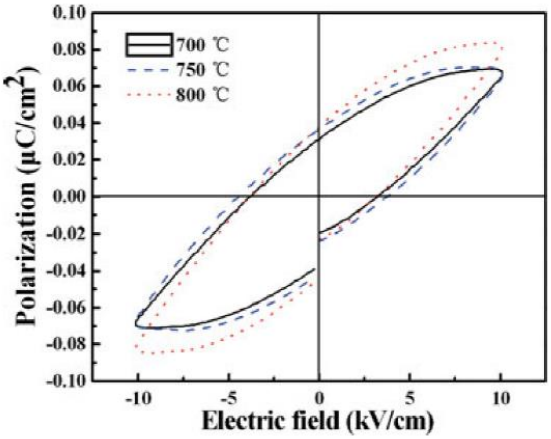

Figure 7: Hysteresis loop for sintered BFO

There is enhanced local conductivity at the domain-walls, much more so than the domains themselves[3]. The conductivity of the walls is related to the kind of domains they separate: 180° walls are the most conductive, followed by 109° walls. The 71° walls don't have any measurable transport enhancement. It is thought that an electrostatic depolarization field may attract charge carriers since polarization normal to the domain

wall does not appear to be constant through it[3]. The Fe-O-Fe bond angle may be responsible for the reduced electronic bandgap for the 180°and 109°domain walls[3].

Figure 8[20] details the measured electrical conductivity and Seebeck coefficients of BFO as a function of partial pressure of oxygen for several elevated temperatures. Schrade et al[20] speculate that there is roughly an equal concentration of electrons and holes since there is minimal dependence of electrical conductivity on the partial pressure of oxygen. The minimal dependence of the Seebeck coefficient on the partial pressure of oxygen indicates that electron holes are the major contributor to the electronic conduction[20].

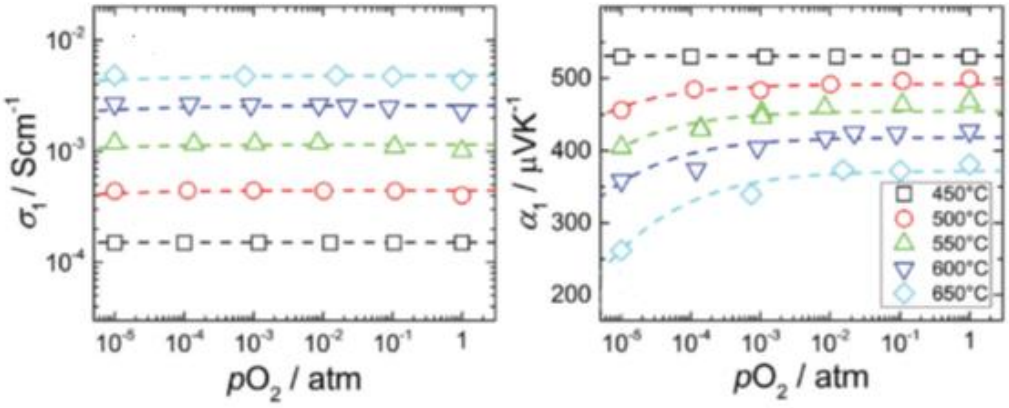

(a) (b)

Figure 8: Electrical conductivity (a) and Seebeck coefficient (b) of BFO with respect to the partial pressure of oxygen

2.1.3. Applications of BFO

Applications for BFO include ferroelectric memory devices[3, 6] and a potential piezoelectric replacement for lead-based materials like PZT[3, 22]. Perovskite solid solutions have also been proposed as cathodes for solid oxide fuel cells (SOFCs) [23]. It has also been evaluated for use as a photovoltaic material[24, 25]. Reports of emitted radiation on the order of terahertz when subjected to a femtosecond laser make BFO a likely candidate for telecommunications and security[3]. In a particularly unique study, Dziubaniuk et al[26] were

able to exploit bismuth ferrite's ammonia sensing properties to develop a safety mechanism for air quality.

Perhaps of most interest, bismuth ferrite has potential device applications in spintronics[6, 27], where memory is written by a voltage and read by a magnetic field. There is a certain appeal to this, since it would require low energy and no moving parts, and reading the memory would be non-destructive (as opposed to ferroelectric memory, where polarization needs to be switched to read it)[3].

2.2. Sintering and Densification of BFO

2.2.1. Review of Sintering

Sintering is a manufacturing technique whereby a material is densified into a solid at temperatures below its melting point. Under conventional sintering, a powder compact is exposed to high temperature ($> 1000℃$) and sometimes pressure (up to the order of GPa) over several hours to promote an increased rate of diffusion and consequently a decrease in porosity of the material. The stages of sintering are shown in Figure 9[28].

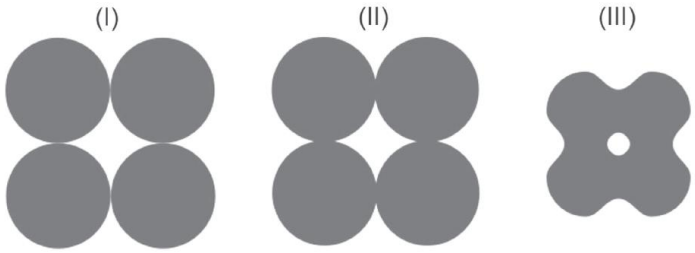

Figure 9: Stages of densification in ceramics. I: Initial Stage with bonded particles, II: Intermediate Stage where shrinkage begins, III: Final Stage with isolated pores and significant shrinkage

Sintering is useful for ceramics since they tend to have very high melting temperatures.

There are six mass transport mechanisms at work during sintering, three of which lead to densification. Figure 10[29] shows these mechanisms and where they take place. Mechanisms 1-3 promote neck growth and do not cause densification. Grain growth occurs

when mass transport takes place from the grain boundaries toward the pores, and this can happen if large pores need to be eliminated, at which point coarsening is possible which inhibits densification.

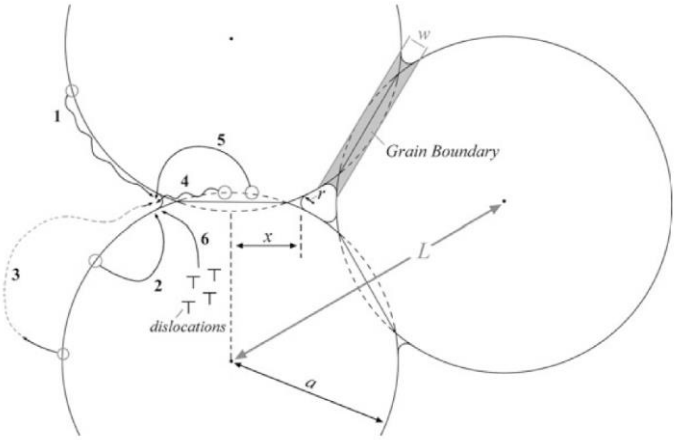

Figure 10: The sintering mechanisms at work and sources of material. Mass transport occurs from the surface by surface diffusion (1), from the surface by bulk diffusion (2), from the surface by evaporation/condensation (3), from the grain boundary by boundary diffusion (4), from the grain boundary by bulk diffusion (5), and from the bulk by bulk diffusion though dislocations (6)

2.2.2. Sintering of BFO

Deng et al[30] conventionally sintered BFO at 800, 820, 850, 880, and 900°C for two hours each, with rapid heating and cooling rates, and found that grain size increases with increasing sintering temperature.

Fu et al[21] conventionally sintered BFO at 700, 750, and 800°C for three hours each to compare crystal structure, surface morphology, dielectric and ferroelectric properties and found that at 800°C impurity phases disappear and single phase $BiFeO_3$ is obtained, having more uniform grains, an increase in dielectric loss, and an increase in remanent polarization.

Dai et al[19] conventionally sintered BFO at 850C in nitrogen, oxygen, and air environments and found that in nitrogen, impurities were minimal, presumably due to the

presence of oxygen vacancies to compensate bismuth vacancies during volatilization. Additionally, they found that leakage current could be minimized when samples were sintered in a nitrogen atmosphere, as shown in Figure 11[19].

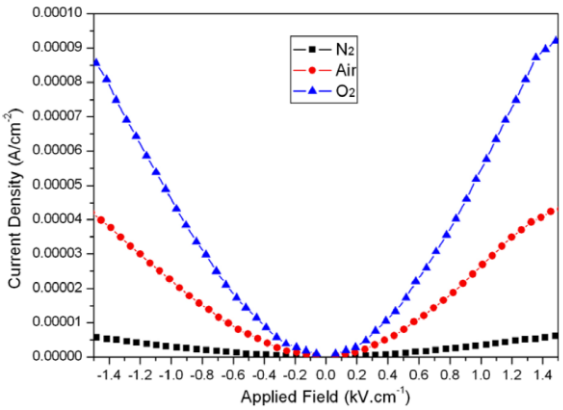

Figure 11: Leakage current as a function of applied electric field for samples sintered in several different environments

Sagdeo et al[31] prepared bismuth ferrite by rapid liquid phase sintering (RLPS) and found that this resulted in better dielectric properties than when samples were annealed after sintering since there were fewer concentrations of impurity phases in the RLPS samples. However, weak ferromagnetism was observed and seems to be an intrinsic property of materials prepared via RLPS[31].

Ponzoni et al[32] were able to densify bismuth ferrite to approximately 95% of theoretical density via a low-temperature (400-800°C) high-pressure (3-8 GPa) sintering technique (LTHP) while avoiding phase degradation and having grain sizes similar to that of the pre-densified powder. Grain growth occurred when the sintering time was increased from 3 minutes to 10 minutes. Dielectric behavior remained unchanged.

When the sintering temperature is too high or too low, bismuth volatilization will produce oxygen vacancies, so the dielectric loss of ceramic samples increases with excessive oxygen vacancy[30].

2.2.2.1. Microwave Sintering of BFO

Microwave sintering refers to the use of microwaves to heat the sample in lieu of conventional heating methods.

Fu et al[33] compared conventional sintering of BFO at 800°C for three hours in air to microwave sintering of BFO at 3kW for 35 minutes in air and found that $Bi_2Fe_4O_9$ impurity phase formed during both processes, but that the grain size of the microwaved sintered BFO was significantly smaller resulting in smaller remanent polarization and higher coercive electric field.

Obulesu et al[34] also compared microwave sintering of BFO to conventional methods and found that structural and dielectric properties were improved for microwave sintered samples.

Cai et al[35] studied the effect of different microwave powers on the properties of BFO ceramics, and found that the ideal power of 3.4 kW was ideal for remanent polarization, coercive field, dielectric loss, and leakage current.

Perejón et al[18] found that both conventionally sintered and microwave sintered pahse-pure BFO samples were electrically insulating at room temperature with resistivity comparable to BFO single-crystal.

2.2.2.2. Field Assisted Sintering of BFO

Since conventional methods require large amounts of energy and time, field assisted sintering techniques (FAST) have been developed to reduce these requirements and enhance sintering.

Recently, pure bismuth ferrite has been spark plasma sintered (SPS)[18, 36, 37, 38]. Wang et al[38] found that magnetization was enhanced and current leakage was minimized

when BFO samples were spark plasma sintered. Perejón et al[18] found that compared to conventional and microwave sintering methods, SPS showed lower resistivity and activation energy when samples were not annealed after the fact.

Several BFO-based composites and doped compounds have also been sintered via SPS[39, 40].

2.3. Flash Sintering

Flash sintering is a relatively new FAST technique: Cologna et al published the first paper detailing it in 2010[41]. They were able to sinter nanograin zirconia at 850°C in less than 5 seconds, much lower than the typical conditions for conventional sintering (1450°C for several hours[41]). The technique is similar to spark plasma sintering (SPS) in that an electric field is applied across the green body, but what differs in flash sintering is that it requires the current to pass through the sample and the electrical requirements become dependent on the material's response to the applied electric field. Insulator ceramics typically need a higher electric field to flash.

In the experimental setup, green bodies are typically sandwiched between two electrodes inside a furnace. Flash sintering can be described in three stages. Stage I is incubation, when the furnace temperature slowly increases. Stage II signifies the onset. This is when a critical furnace temperature is met such that the sample conductivity increases, causing a rapid increase in current, which heats up the sample further. It is when this thermal runaway occurs that densification begins. In the final stage, the power supply goes from voltage controlled to current controlled as a result of enhanced conductivity in specimen. Figure 12[42] shows an example of this process in terms of electric field, current density, power density, and linear shrinkage strain versus time.

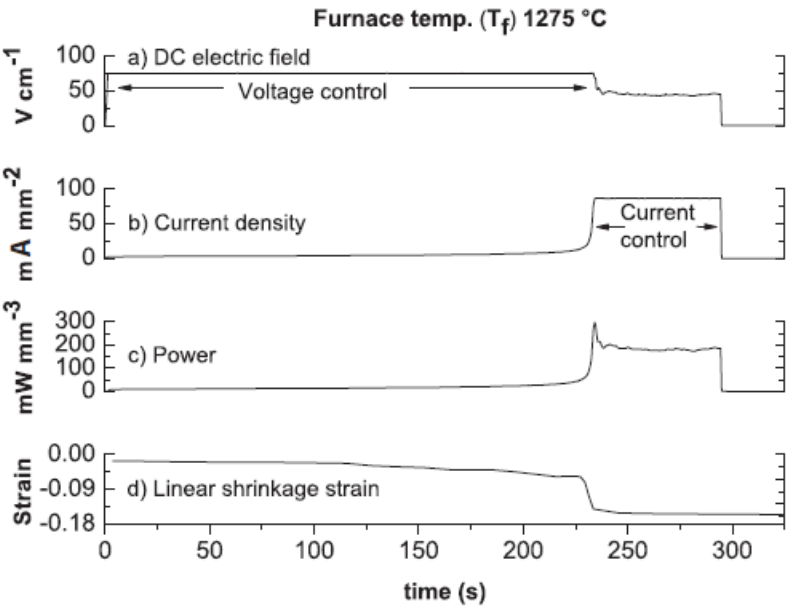

Figure 12: Isothermal flash sintering versus time curves for (a) DC electric field, (b) current density, (c) power, and (d) linear shrinkage strain for alumina-3YSZ composite at 1275℃ for 75 V/cm

Flash sintering experiments can be isothermal or nonisothermal. An isothermal experiment involves heating the furnace to the desired temperature, at which point the electric field is applied. A nonisothermal experiment consists of applying the electric field while the furnace continues to heat up until it goes into flash state.

Research in this field has focused on three areas: identifying materials to flash sinter, varying the experimental setup, and determining the underlying mechanisms of flash sintering[43].

Since Cologna's work, flash sintering has been investigated for a variety of oxide, non-oxide, and composite materials under both AC and DC fields[28, 43] (see Table 4). A few of them can be seen in Figure 13 [44].

Table 4: Materials that have been flash sintered

doped and undoped alumina[45, 46]	potassium niobate[47]
Al_2O_3/TZP composites[48]	silicon carbide[49, 50]
alumina-titania[51]	$SrTi_{1-x}Fe_xO_3-\delta$[52]
alumina-YSZ[42, 53]	strontium titanate[54, 55]
barium titanate[56, 57]	tin dioxide[58]
$CaCu_3Ti_4O_{12}$[59]	doped and undoped titania[60, 61, 62]
doped and undoped ceria[63, 64, 65, 66, 67]	doped and undoped yttria[68, 69, 70]
cobalt manganese oxide[71]	yttria-stabilized zirconia (YSZ)[72, 73, 74, 75]
$La_{0.6}Sr_{0.4}Co_{0.2}Fe_{0.8}O_3$ (LSCF)[76]	zinc oxide[77, 78, 79, 80]
magnesium aluminate[81]	zirconia[41, 82, 83]
manganese cobaltite[84]	

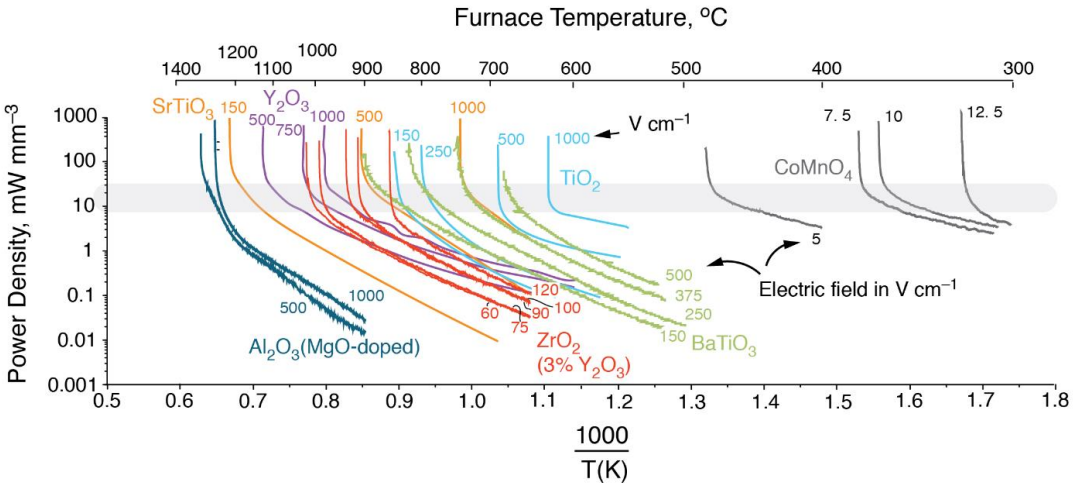

Figure 13: Power density vs furnace temperature for several materials

There has been much disagreement regarding the possible mechanisms for flash sintering. Arguments have been made for the local heating of grain boundaries, the nucleation of avalanches of lattice defects, and thermal runaway[43, 85], but none have gained widespread acceptance as yet. Details of these possible mechanisms are discussed in further detail in Chapter 7.

Many experimental setups for flash sintering have been tested and evaluated. Common variations on Cologna's setup are listed in Table 5:

:

Table 5: Variations on Flash Sintering Experiments

Parameter	Variations
Specimen dimensions	Dogbone, button or disc, etc.
Furnace type	Tube furnace, custom design, etc.
Electrode type	Wires, plates, pastes, etc.
Electric field	AC or DC
Temperature conditions	Isothermal or nonisothermal

As of yet, there has been limited study on material properties of flash sintered ceramics[85].

2.3.1. Flash Sintering of BFO

The first instance of flash sintering of bismuth ferrite was conducted by Pérez-Maqueda et al[86], and they showed that flash sintering aids in preserving the phase purity and composition. Their sample of BFO was flashed at 100 V/cm and 20 mA/mm^2 which resulted in no loss of BFO and an average grain size of 20 nm with low porosity.

Gil-González et al [87] were subsequently able to produce phase-pure bulk BFO by reaction flash sintering BiO_2 and FeO_2 powders in air at 625°C in a matter of seconds.

3. THESIS OBJECTIVE

3.1. Scope

Bismuth ferrite is typically sintered near 1000℃ and has a Curie temperature below 900℃. It is of great interest to flash sinter this material, not only to compare results against conventional sintering methods, but to also evaluate the feasibility of flash sintering below BFO's Curie temperature to avoid phase transitions which act against densification during sintering. If flash sintering below the Curie temperatures proves to be successful for bismuth ferrite, it can potentially open up many applications that make use of its piezoelectricity, magnetoelectricity, and spintronic properties[3, 88] for a class of materials that could not be made as robustly in bulk previously.

While rapid sintering at lower temperature and with little grain growth is an important technical advantage, determining the mechanisms behind flash sintering of ferrites is also essential. X-ray diffraction is one of the most widespread known techniques for understanding the change in structure. But in a typical lab x-ray diffraction setup, the beam energy is not enough to penetrate bulk materials, and the beam intensity does not allow for very rapid data acquisition.

Using high energy dispersive x-ray diffraction (EDXRD) *in situ*, we can study sintering behavior while it occurs since the penetration depth is large enough for the beam to pass through the furnace. This technique allows us to track phase transformations and the temperature of the specimen. We can analyze this information and explain general flash sintering phenomena, which will help resolve the diverging theories.

3.1.1. Densification of BFO

BFO was flash sintered to high density with minimal grain growth.

3.1.2. Comparison of Densification at Different Temperatures & Electric Fields

It is important to ascertain how different furnace temperatures and electric fields affect flash sintering of bismuth ferrite to determine ideal flash conditions. It is also of interest to determine whether flash sintering of BFO is comparable to conventional methods in terms of resulting properties.

3.1.3. Estimating Sample Temperature

We want to reliably estimate sample temperature to better understand what happens during flash sintering and to confirm that any adverse phase transitions are avoided.

3.1.4. Identifying and Quantifying Mechanisms of Flash Sintering

Several mechanisms for flash sintering have been proposed, but none have gained widespread acceptance. This is partially due to the fact that mechanisms are dependent on the material being flashed and can vary greatly. Some mathematical models have been developed based on nucleation and growth, Frenkel defect avalanche, and Joule heating. It is of interest to apply these models to BFO to determine what the likely mechanisms are for flash sintering this material.

4. EXPERIMENTAL METHODS

4.1. Sample Preparation

Bismuth ferrite powder was developed via mechanosynthesis[89]. The initial powder is shown in Figure 14. Green bodies are compacted using an Across International pellet press with cylindrical dies in our laboratory. Pressures up to 1 MPa are applied to achieve between 50% and 70% of the theoretical density. Pellets are 6mm wide and typically 5mm thick. Depending on the desired furnace temperature, either silver or platinum paste is applied to the circular sides of the samples and cured. The cured paste acts as an electrode on either side of the sample, and they are connected to a power supply via platinum wires (as platinum can withstand high temperature without being oxidized).

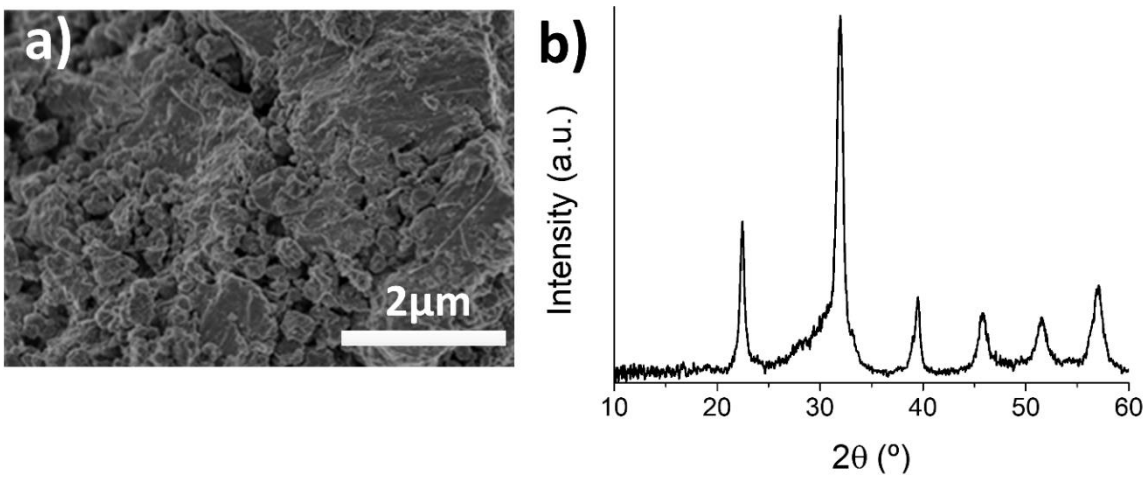

Figure 14: Milled BFO powder (a), XRD pattern of the milled sample (b). SEM completed by Pérez-Maqueda group at CSIC-Univ. de Sevilla

4.2. Flash Sintering Furnace

The experiments discussed in this dissertation implemented a first-generation portable furnace developed by the Nanomaterials Laboratory that was subsequently modified (see Figure 15).

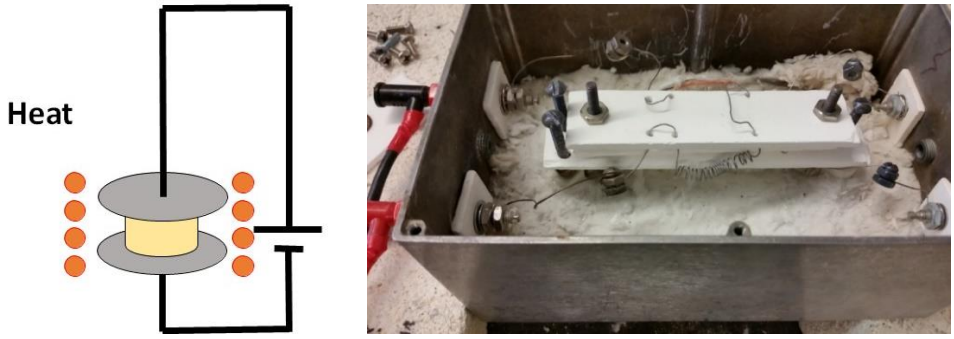

(a) (b)

Figure 15: Schematic of sample (a), photograph of furnace interior with modified heating coils (b)

To conduct an experiment, the pellet was coated on top and bottom with a platinum paste that functions as electrodes. The heating coils of the furnace have a separate power supply (BK Precision 9115 DC) which was turned on to increase the furnace temperature, with a feedback system of a K-type thermocouple placed close to the sample. When the desired temperature was reached during an isothermal experiment, an electric field was applied through the electrodes to the sample, controlled by a BK Precision PVS DC power supply.

4.3. X-Ray Diffraction (XRD)

X-ray diffraction (XRD) is a technique used to analyze the structure and phase of a crystalline material based on its lattice parameters. In traditional XRD, a certain wavelength of X-rays passes through a sample and a goniometer changes the angle of the detector to determine the diffraction pattern of individual crystal faces.

The governing equation for XRD is Bragg's Law:

$$n\lambda = 2d_{hkl} \sin\theta \qquad (7)$$

where $n =$ a positive integer, $\lambda =$ wavelength, $d_{hkl} =$ the interplanar spacing of the (hkl) reflection in Angstroms, and $\theta =$ the detector angle. Figure 16 shows how this equation

comes into play. If beams of identical wavelength are scattered off of two different particles, the lower beam travels an extra length of $2d_{hkl}\sin\theta$. Constructive interference occurs when that value is equal to the wavelength or a multiple of it.

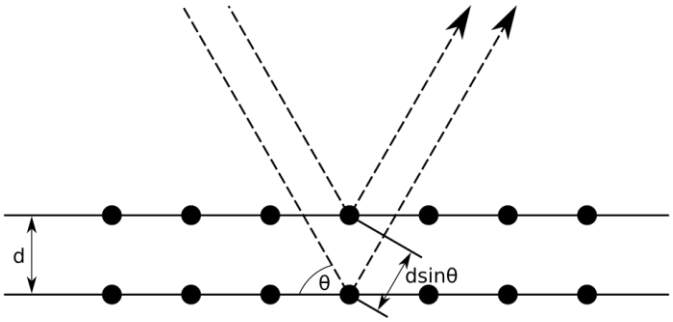

Figure 16: Schematic of Bragg diffraction

4.3.1. Synchrotron Radiation

EDXRD experiments require synchrotron radiation. A synchrotron facility is a large ring in which electrons are emitted from a cathode at high temperature and are injected into the ring. The electrons are radially accelerated via several radio frequency cavities to speeds approaching that of light. The path of the electrons is maintained via bending magnets. The excited electrons release massive amounts of energy as photons. Beamlines are set up at tangent points around the ring that capitalize on various electromagnetic spectra for experiments according to application.

4.3.2. Energy Dispersive X-Ray Diffraction (EDXRD)

Energy dispersive x-ray diffraction (EDXRD) differs from traditional XRD in that the angle of the detector is kept constant and a wide range of x-ray wavelengths pass through the sample. This allows for diffraction data to be acquired for all relevant crystal faces simultaneously. Since a goniometer is therefore not required, and the intensity of the x-rays is very high, data can be acquired much quicker compared to traditional XRD.

Moreover, the x-ray energies are so high that deep penetration through solid materials is possible.

The governing equations for EDXRD are Bragg's Law and Planck's equation,

$$E = hv \tag{8}$$

where $E =$ energy in eV, $h =$ Planck's constant $= 4.135 \times 10^{-35}$ eV, $v =$ frequency $= c/\lambda$ (where $c =$ speed of light $= 2.9979 \times 10^{8}$ m/s). Solving Eqs (7) and (8) for wavelength and setting them equal to each other, we get:

$$\frac{2d_{hkl}\sin\theta}{n} = \frac{hc}{E_{hkl}}$$

or

$$E_{hkl} = \frac{hc}{2d_{hkl}\sin\theta} \tag{9}$$

Substituting constant values into Eq (9), we have an equation for the scattered energy of the (hkl) reflection in keV:

$$E_{hkl} = \frac{6.1992}{d_{hkl}\sin\theta} \tag{10}$$

4.3.3. In-situ Analysis

Shown in Figure 17, the synchrotron facility at Argonne National Laboratory is known as the Advanced Photon Source (APS).

Figure 17: The Advanced Photon Source at Argonne National Laboratory

The 6 BM-A beamline delivers photons with energies up to 200 keV via a superconducting wiggler. The EDXRD setup at 6 BM-A is shown in Figure 18:

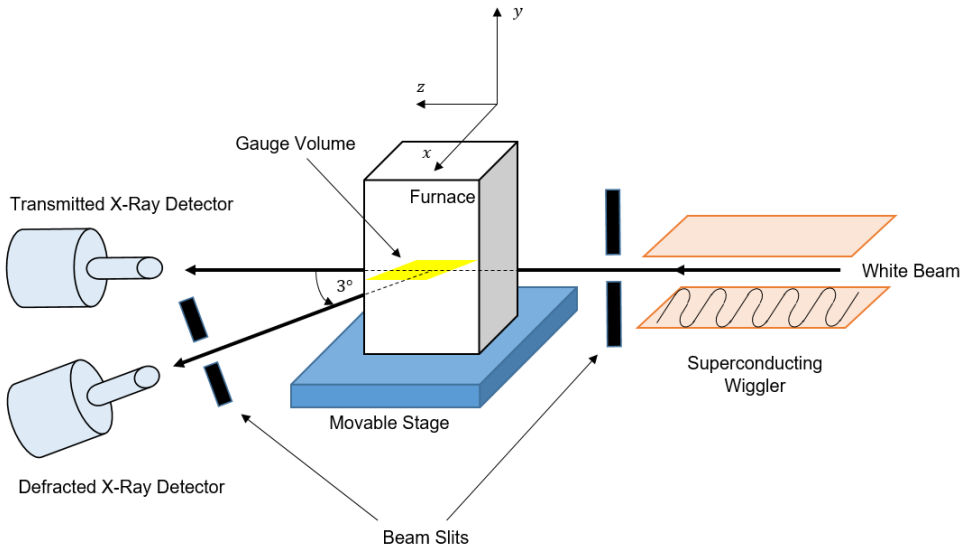

Figure 18: Schematic of beamline at 6 BM-A

A white x-ray beam is generated through the wiggler and passes through the sample gauge volume (shown in yellow), whose position is controlled by a three-axis sample stage. The gauge volume is a parallelepiped whose size is dependent on the size of the incident beam collimation slits and the Bragg angle. The diffracted beam is recorded at a fixed Bragg angle $2\theta = 3°$. Higher Bragg angles reduce the intensity of the beam.

Photographs of the detector and beamline at 6 BM-A are show in Figure 19:

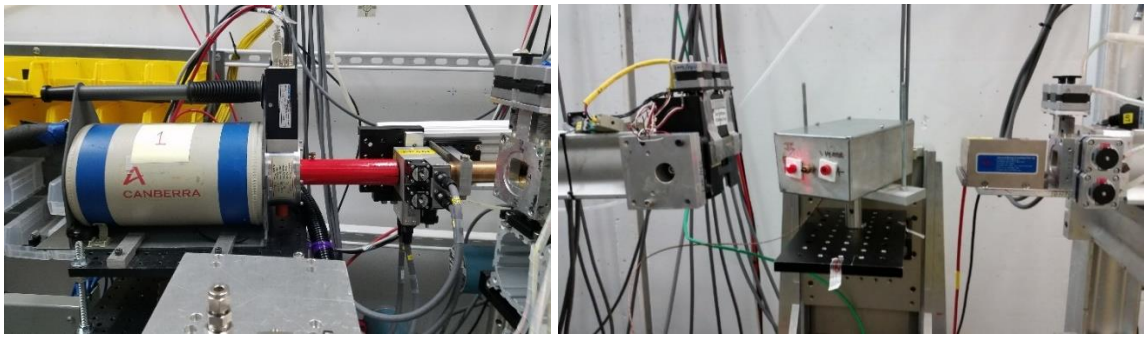

Figure 19: Photographs of 6 BM-A. The first photograph shows the diffracted X-ray detector which is offset by 3° from the horizontal. The second photograph shows the sample stage with the furnace installed. The X-ray beam enters the furnace from the right.

4.3.4. Energy Calibration and Data Analysis

Energy calibration for EDXRD was carried out with ceria and alumina standards to account for instrumental error. The XRD spectra are represented by the germanium detector as channel numbers. These channels correspond to certain energy levels which can be mapped to known interplanar spacings of the standards. Channels 0 through 8192 correspond to 0 through 200 keV. A linear calibration curve is used to map the channels to energy. The one for alumina is shown in Figure 20.

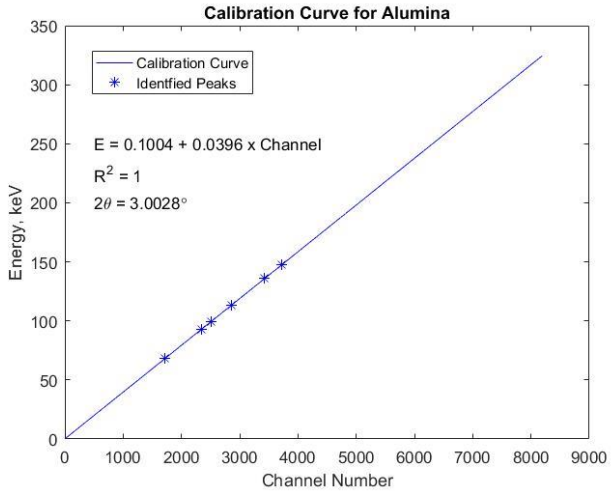

Figure 20: Calibration curve for alumina to determine energy in keV

The interplanar spacing for the (104) and (110) reflections of BFO were identified using the ICDD standard for BFO (see Figure 21[90]). The interplanar spacings were then used to calculate hexagonal lattice parameters.

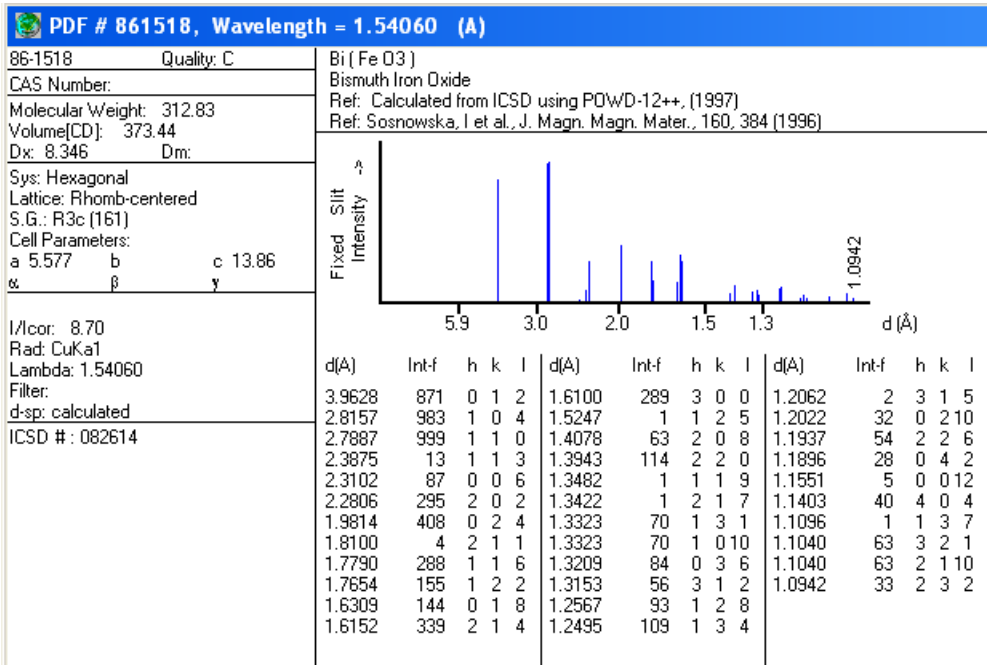

PDF # 861518, Wavelength = 1.54060 (A)

86-1518 Quality: C
CAS Number:
Molecular Weight: 312.83
Volume[CD]: 373.44
Dx: 8.346 Dm:
Sys: Hexagonal
Lattice: Rhomb-centered
S.G.: R3c (161)
Cell Parameters:
a 5.577 b c 13.86
α β γ
I/Icor: 8.70
Rad: CuKa1
Lambda: 1.54060
Filter:
d-sp: calculated
ICSD # : 082614

Bi (Fe O3)
Bismuth Iron Oxide
Ref: Calculated from ICSD using POWD-12++, (1997)
Ref: Sosnowska, I et al., J. Magn. Magn. Mater., 160, 384 (1996)

Fixed Slit Intensity

1.0942

5.9 3.0 2.0 1.5 1.3 d (Å)

d(A)	Int-f	h	k	l	d(A)	Int-f	h	k	l	d(A)	Int-f	h	k	l
3.9628	871	0	1	2	1.6100	289	3	0	0	1.2062	2	3	1	5
2.8157	983	1	0	4	1.5247	1	1	2	5	1.2022	32	0	2	10
2.7887	999	1	1	0	1.4078	63	2	0	8	1.1937	54	2	2	6
2.3875	13	1	1	3	1.3943	114	2	2	0	1.1896	28	0	4	2
2.3102	87	0	0	6	1.3482	1	1	1	9	1.1551	5	0	0	12
2.2806	295	2	0	2	1.3422	1	2	1	7	1.1403	40	4	0	4
1.9814	408	0	2	4	1.3323	70	1	3	1	1.1096	1	1	3	7
1.8100	4	2	1	1	1.3323	70	1	0	10	1.1040	63	3	2	1
1.7790	288	1	1	6	1.3209	84	0	3	6	1.1040	63	2	1	10
1.7654	155	1	2	2	1.3153	56	3	1	2	1.0942	33	2	3	2
1.6309	144	0	1	8	1.2567	93	1	2	8					
1.6152	339	2	1	4	1.2495	109	1	3	4					

Figure 21: ICDD standard for BFO

These two peaks appear very close to each other, so getting a good fit with deconvolution is difficult. The peak breadth was determined by manually identifying the peaks and fitting them with a Gaussian function using fityk[91]. The XRD spectra was additionally fit using a pseudo-Voigt function in MATLAB developed by the Nanomaterials Laboratory at Rutgers.

5. FLASH SINTERING OF BISMUTH FERRITE

Three samples of BFO were analyzed at Argonne National Laboratory. One sample was pre-sintered, and the other two were green compacts. Each sample underwent several flash sintering experiments to maximize time use at APS. Two types of EDXRD scans were taken. Regular Scans (RS) consist of one XRD profile taken every three seconds. This enables us to monitor and analyze changes in the XRD pattern. Long Scans (LS) consist of one XRD profile for 300 seconds. This enables us to have XRD patterns with higher intensity.

5.1. Pre-sintered sample flashed at 650℃

The experimental scans for the pre-sintered sample at 650°C are shown in Figure 22, where regular scans are shown in red and long scans are in blue:

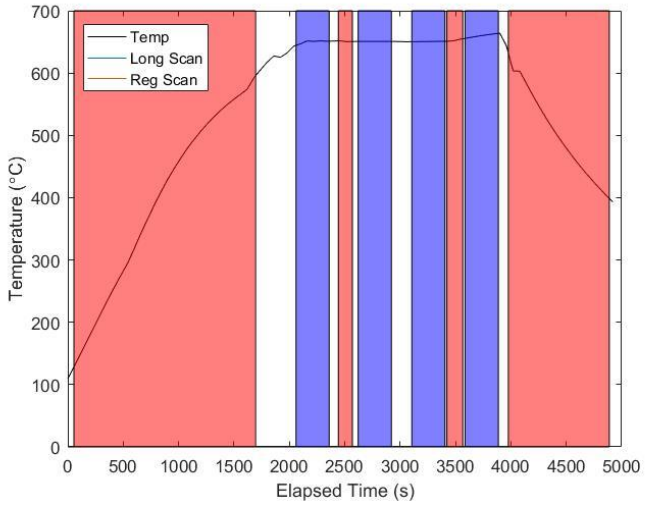

Figure 22: Experiment Runs for Pre-Sintered Sample at 650°C

The first and last regular scans recorded spectra without any presence of an electric field as the furnace temperature increased and decreased, respectively. The first flash experiment was conducted with an electric field of 50 V/cm and a current density of 2.5 A/cm^2. The

subsequent flash experiment was conducted with an electric field of 24 V/cm and a current density of 5 A/cm^2.

Figure 23 shows the changes in energies and interplanar spacing for the (104) and (110) reflections during temperature ramp-up (first regular scan). The plots are enlarged since the two peaks are so close together.

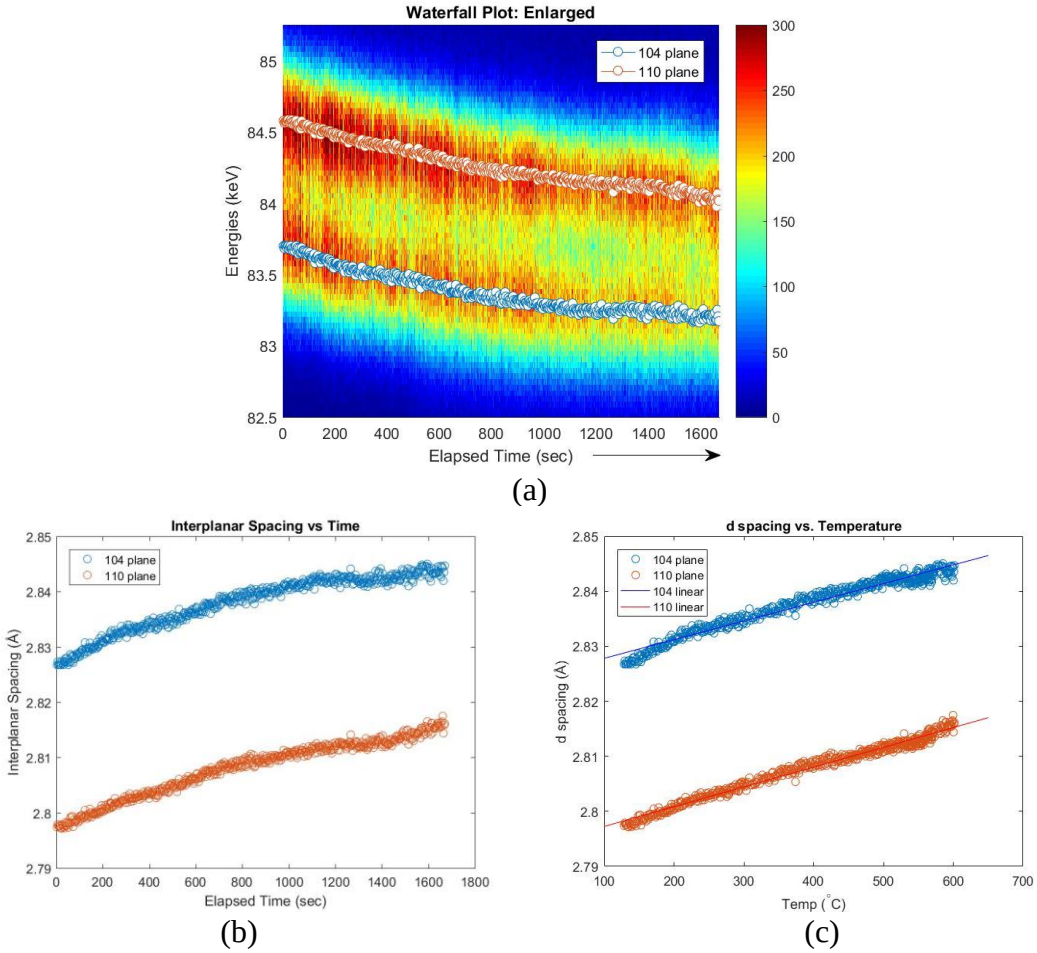

Figure 23: Baseline energies (a) and interplanar spacing (b) versus time during temperature increase. Interplanar spacing versus temperature (c)

The decrease in peak energies and increase in interplanar spacings are consistent with thermal expansion[92]. Figure 23c shows the interplanar spacing with respect to temperature to account for variations due to manual temperature control.

Hexagonal lattice parameters were calculated from the interplanar spacing. While there is some variation beyond 500°C, Figure 25 shows that for the most part, the hexagonal lattice expansion occurs linearly.

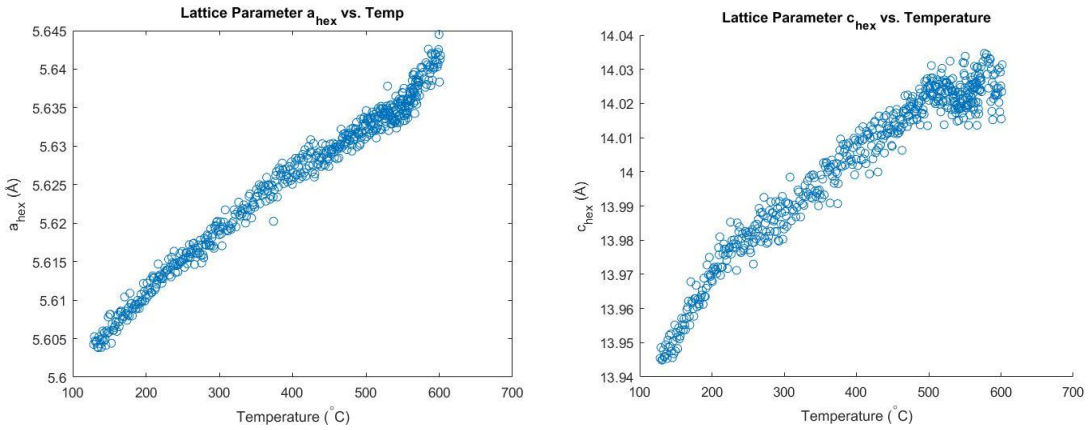

Figure 24: Changes in hexagonal lattice parameters due to temperature increase

Figure 25 shows the normalized hexagonal lattice parameters, confirming that lattice expansion occurs at a relatively similar rate.

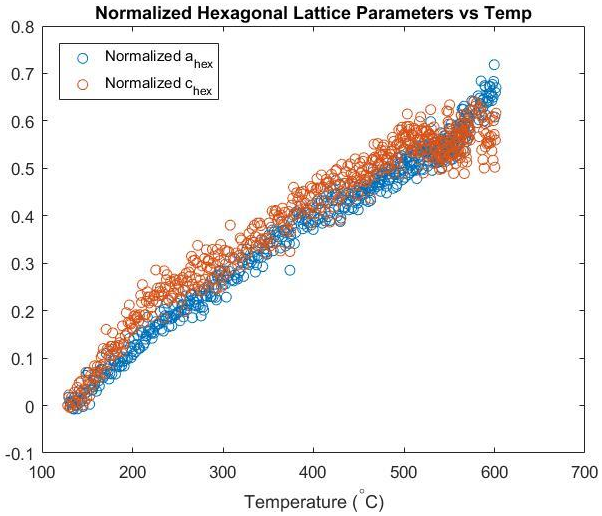

Figure 25: Normalized hexagonal lattice parameters

Once the target temperature of 650°C was reached, a long scan was taken to see the peaks more clearly since bismuth is very absorptive and attenuates the X-ray beam (see Figure

26). As mentioned, peaks (104) and (110) were identified using the ICDD standard in Figure 21.

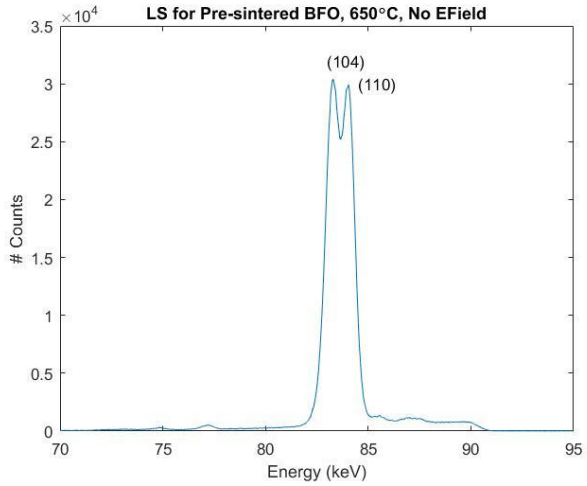

Figure 26: Long scan with peak identification at 650°C

Once the peak locations at 650°C were established, the first flash experiment was started. Figure 27a shows the electric field, current density, and power density versus time for the first flash experiment. Flash sintering began at 67 seconds and lasted for sixty seconds. The incubation, onset, and transient stages of flash are apparent.

Figure 27b shows a horizontal waterfall plot of the peak energies with respect to time. During Stage II of flash sintering, it appears that one of the peaks disappears, or, more accurately, merge into a single peak. The fact that the (104) and (110) peaks combine signifies that an unwanted phase transformation from rhombohedral to orthorhombic has occurred. That is, the sample exceeded the Curie temperature of 825°C during the flash experiment and became paraelectric. While this process is reversible, it does act against proper densification. The single peak after the phase transformation corresponds to the orthorhombic (112) peak.

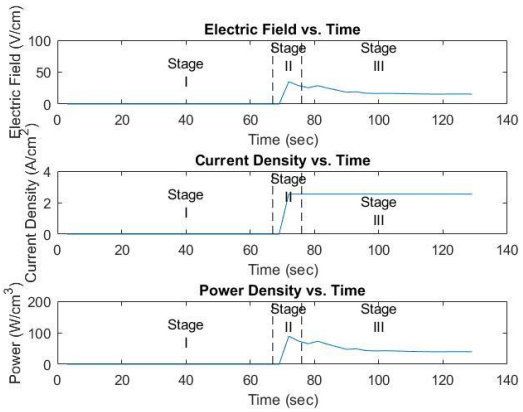

(a)

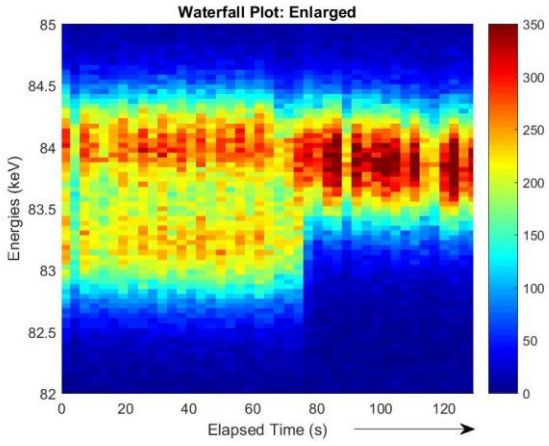

(b)

Figure 27: Electric field, current density, and power density versus time (a) and peak energies versus time (b) for a flash experiment conducted at 650°C, 50 V/cm and 2.5 A/cm²

After several flash experiments at 650°C, it was found that at a high current density, the sample decomposed into its liquid state, as evidenced by the addition of several peaks (see Figure 28). This decomposition is consistent with findings in literature[11].

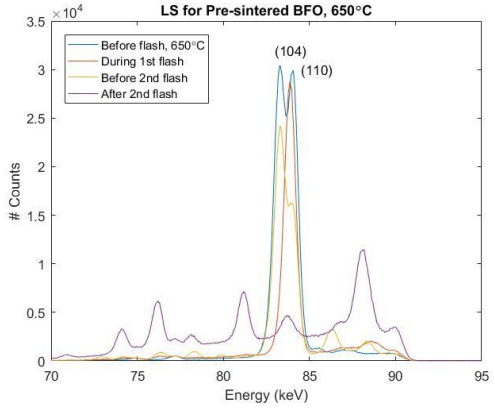

Figure 28: Long scans of BFO at 650C showing eventual decomposition

5.2. Green compact flashed at 500℃

The experimental scans for the green compact sample at 500°C are shown in Figure 29:

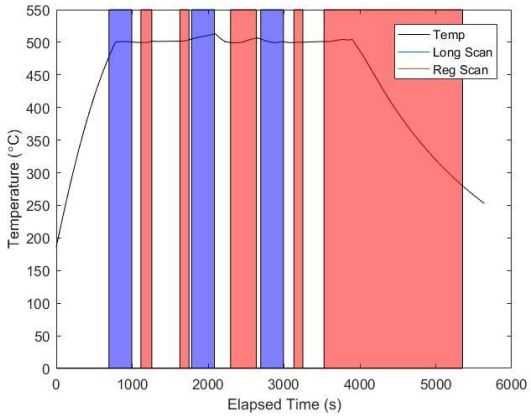

Figure 29: Experimental Runs for Green Compact Sample at 500°C

First, a long scan at 500°C was taken to establish peak locations at that temperature. The sample was subsequently flashed four times with constant electric fields of 40 and 60 V/cm and current densities of 1 and 2 A/cm^2. A regular scan was taken during temperature ramp down as well.

Once the target temperature of 500°C was approximately reached, the long scan was taken to see the peaks more clearly (see

Figure *30*):

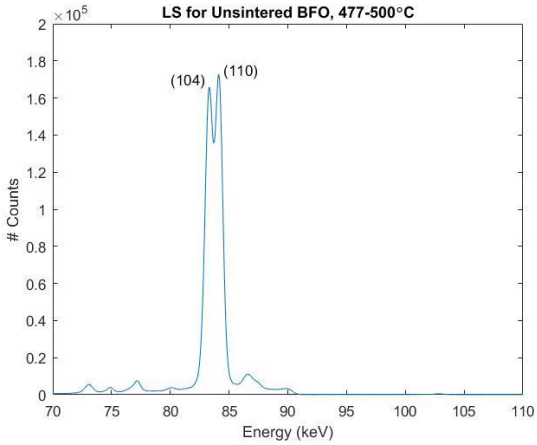

Figure 30: Long scan for green compact BFO at 500°C

Figure 31a shows the electric field, current density, and power density versus time for the first flash experiment at 500°C. Flash sintering began at 111 seconds and lasted for thirty seconds. The incubation, onset, and transient stages of flash are apparent.

Figure 31b shows a horizontal waterfall plot of the peak energies with respect to time. The energies decrease suddenly during Stage II, but the peaks remain separate. The fact that they do signifies that a phase transformation from rhombohedral to orthorhombic has not occurred. That is, the sample has remained below the Curie temperature during the flash experiment. Figure 31c shows the corresponding interplanar spacing versus time obtained from Equation (10).

Perhaps more intriguing is the nature of the peak shifts. It appears from Figure 31b that the (110) peak shifts to a lower energy at a different rate than the (104) peak. The calculated changes in hexagonal lattice parameters are shown in Figure 32. If we normalize the hexagonal lattice parameters (see Figure 33) the change in a_{hex} is more drastic than c_{hex} although the increase is still visible. At this point, it remains unclear whether this is an artifact of the convolution of peaks or whether the electric field causes an anisotropic lattice expansion effect.

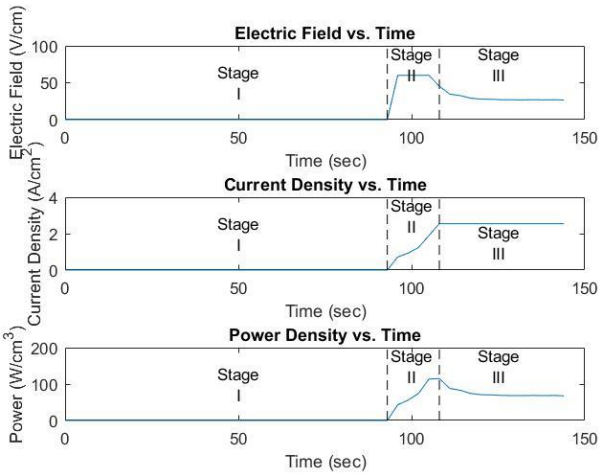

(a)

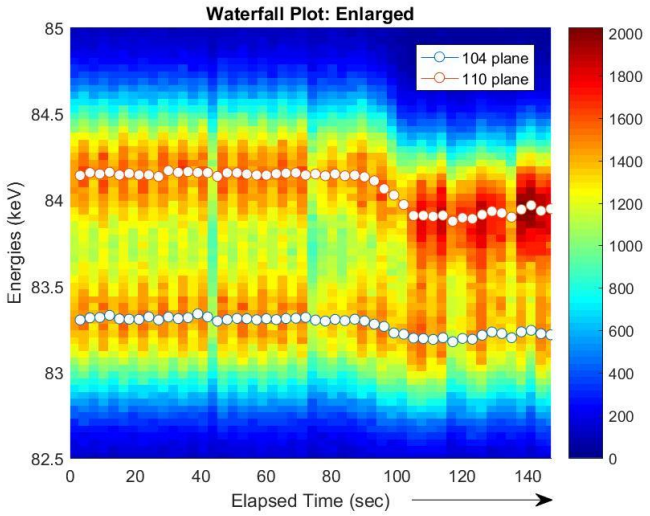

(b)

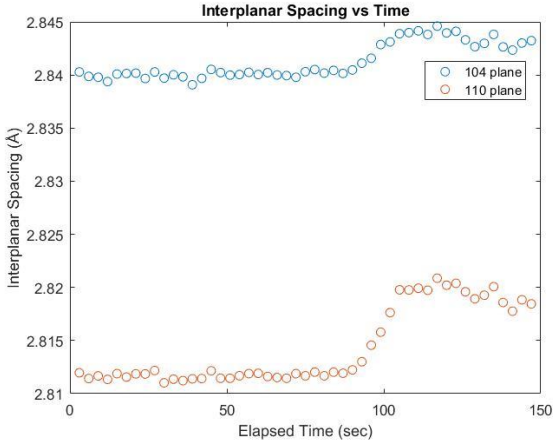

(c)

Figure 31: Electric field, current density, and power density versus time (a), peak energies versus time (b), and interplanar spacing versus time (c) during flash at 500°C

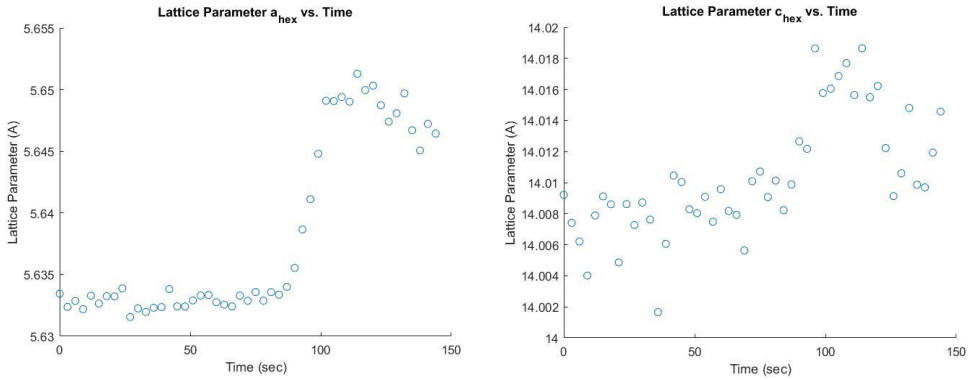

(a) (b)

Figure 32: Change in hexagonal lattice parameters during flash at 500°C.

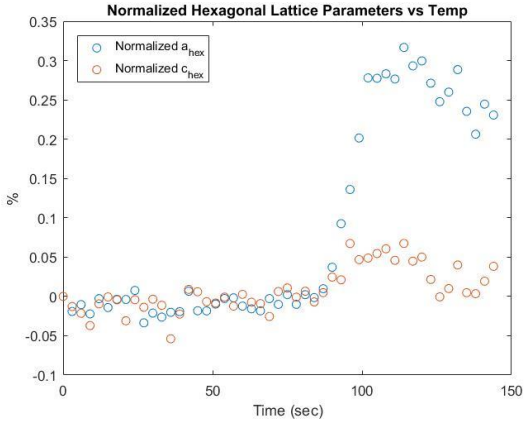

Figure 33: Normalized hexagonal lattice parameters versus time during flash at 500°C

The change in full width at half maximum (FWHM) is shown in Figure 34. The general trend shows a narrowing of the peaks which is to be expected[92, 93].

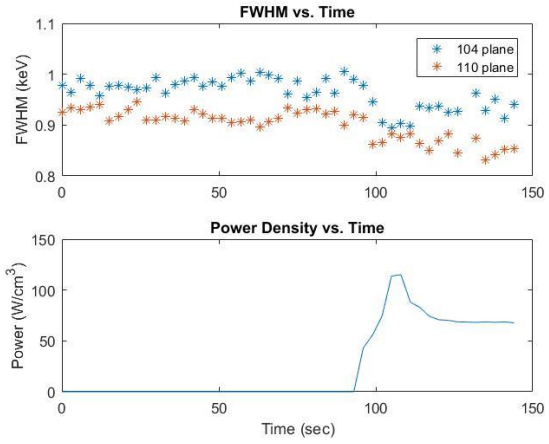

Figure 34: FWHM versus time during the flash event

While the sample was still undergoing flash, a long scan was taken during Stage III. Compared to the pre-sintered long scan (see Figure 35), it appears that the (104) peak remains relatively in place while the (110) peak has shifted slightly to the left. For conventional sintering, we would expect similar peak shifts for both peaks. This unusual behavior confirms that the lattice changes are not an artifact of the pseudo-Voigt fit but an effect of the sample's exposure to an electric field.

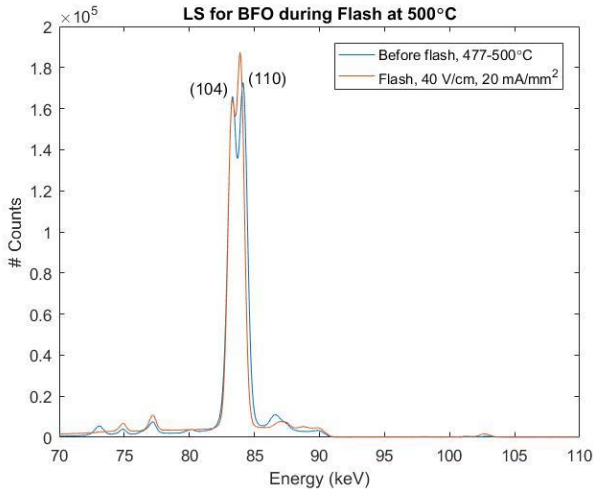

Figure 35: Long scan comparison during transient period of flash at 500°C

Figure 36 shows an SEM comparison of densified BFO to the original milled powder. The dense BFO has low porosity, having reached approximately 90% of the theoretical density, and little if any grain growth.

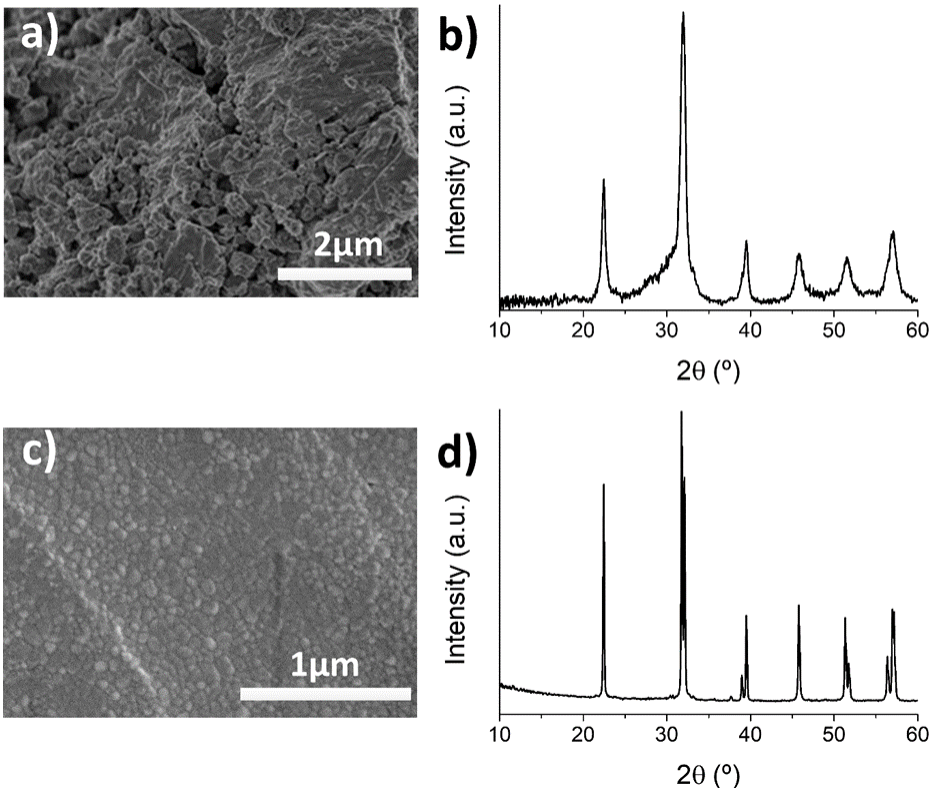

Figure 36: An indication of densification: Milled $BiFeO_3$ powder (a), XRD pattern of the milled sample (b), densified $BiFeO_3$ at a furnace temperature of 500°C (c), and XRD pattern of the densified $BiFeO_3$ (d). SEM completed by Pérez-Maqueda group at CSIC-Univ. de Sevilla

Subsequent flash experiments were run at 500°C, however the change in electric field primarily resulted in significant grain growth, which inhibits densification as well.

5.3. Green compact flashed at 350℃

The experimental scans for the green compact sample at 350°C are shown in Figure 37:

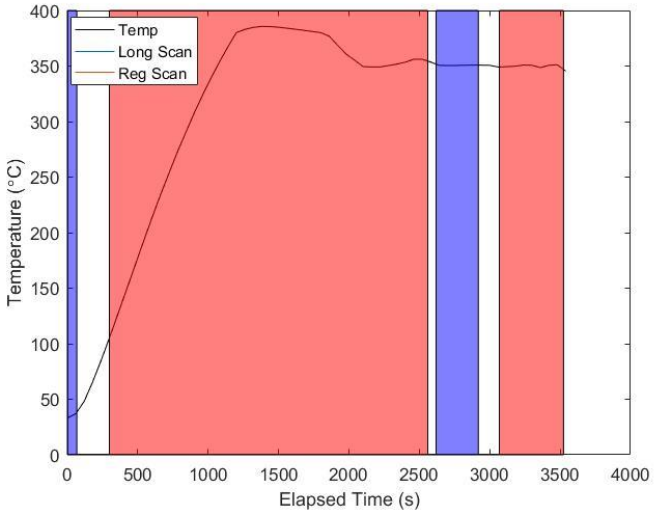

Figure 37: Experiment Runs for Green Compact Sample at 350°C

Two long scans were taken, once at room temperature and another after the first flash. The bump in the temperature plot is due to manually tuning the furnace temperature via a power supply. Once the temperature was corrected, the sample was flashed at 80 V/cm and 2.5 A/cm^2. The same sample was subsequently flashed two more times at electric fields of 90 and 150 V/cm, respectively, and current density of 2.5 A/cm^2.

Figure 38a shows the electric field, current density, and power density versus time for the first flash experiment. Flash sintering began at 2166 seconds and lasted for one hundred seconds. The incubation, onset, and transient stages of flash are apparent.

Figure 38b shows a horizontal waterfall plot of the peak energies with respect to time. Again, the sample remained below the Curie temperature during the flash experiment. Figure 38c shows the corresponding interplanar spacing versus time obtained from

Equation (10). Due to the long period for temperature to reach equilibrium, Figure 38 is truncated before 1900 seconds.

It appears from Figure 38b that the (110) peak shifts to a lower energy at a different rate than the (104) peak, the same behavior we saw at 500°C. The calculated changes in hexagonal lattice parameters are shown in Figure 39. If we normalize the hexagonal lattice parameters (see Figure 40) the change in a_{hex} is more drastic than c_{hex} although the increase is still visible.

The change in full width at half maximum (FWHM) is shown in Figure 41. The general trend shows a dramatic narrowing of the peaks at flash.

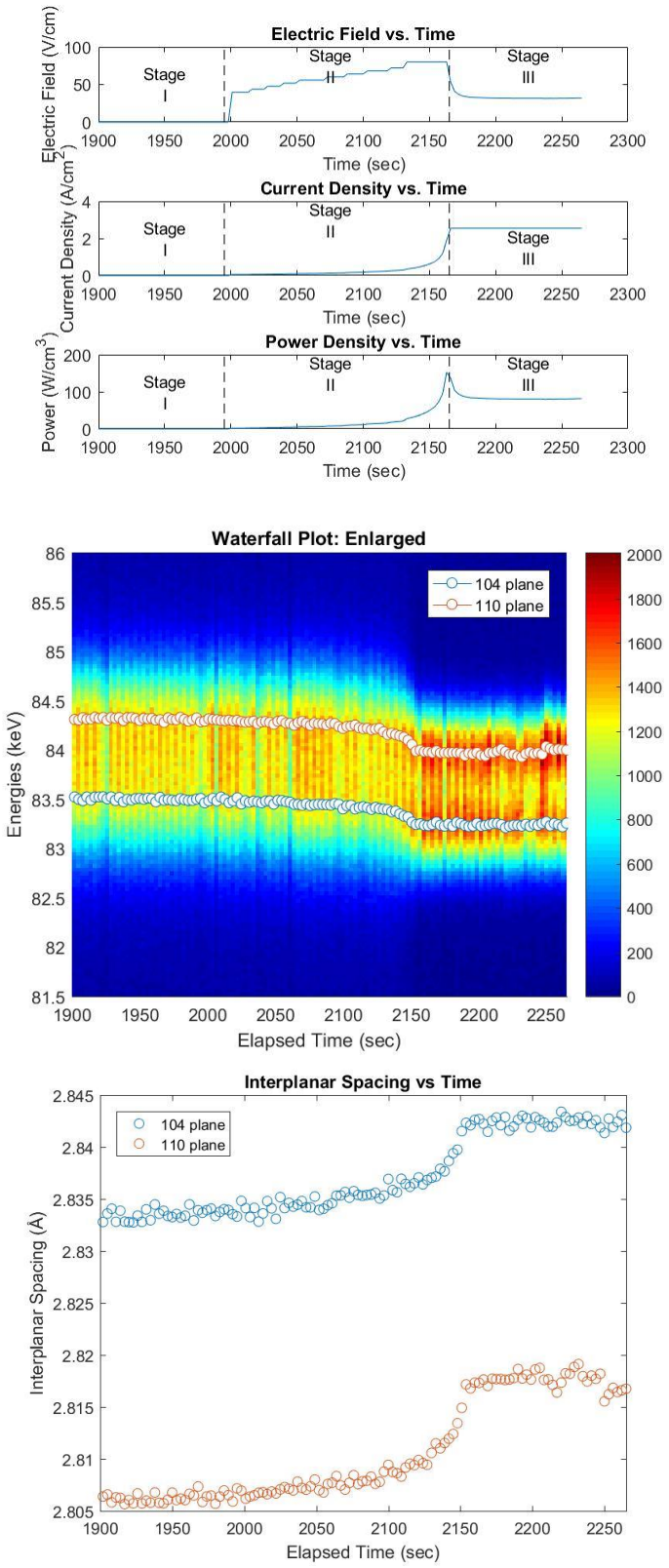

Figure 38: Electric field, current density, and power density versus time (a), peak energies versus time (b), and interplanar spacing versus time (c) for flash sintering at 350°C

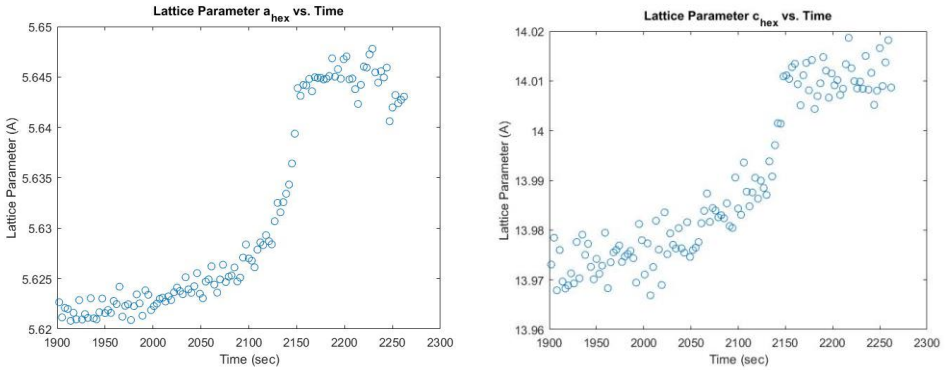

Figure 39: Change in hexagonal lattice parameters during flash at 350°C

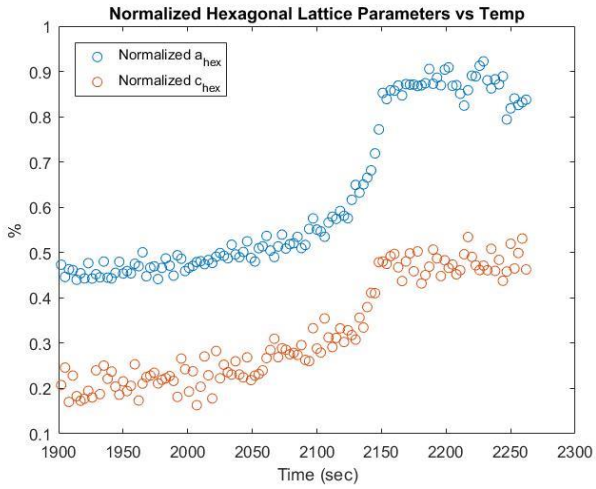

Figure 40: Normalized hexagonal lattice parameters versus time during flash at 350°C

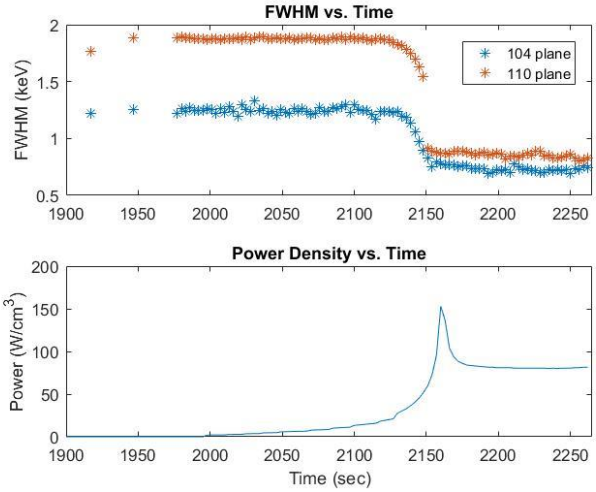

Figure 41: FWHM versus time during the flash event

Figure 42a shows the electric field, current density, and power density versus time for the second and third flash experiments. Flash sintering began at 138 seconds and lasted for 140 seconds, and began again at 357 seconds and lasted 72 seconds. The incubation, onset, and transient stages of flash are apparent both times.

Figure 42b shows a horizontal waterfall plot of the peak energies with respect to time. The shape of the Again, the sample remained below the Curie temperature during the flash experiment. Figure 42c shows the corresponding interplanar spacing versus time obtained from Equation (10).

It appears from Figure 42b that again, the (110) peak shifts to a lower energy at a different rate than the (104) peak. The calculated changes in hexagonal lattice parameters are shown in Figure 43. If we normalize the hexagonal lattice parameters (see Figure 44) the change in a_{hex} is more drastic than c_{hex} although the increase is still visible.

The change in full width at half maximum (FWHM) is shown in Figure 45. The general trend shows minimal narrowing of the peaks at flash. This is likely because the sample was flashed already.

It should be noted that the shape of the graphs in Figure 42b and c are due to manual temperature control and are not from any electric field exposure.

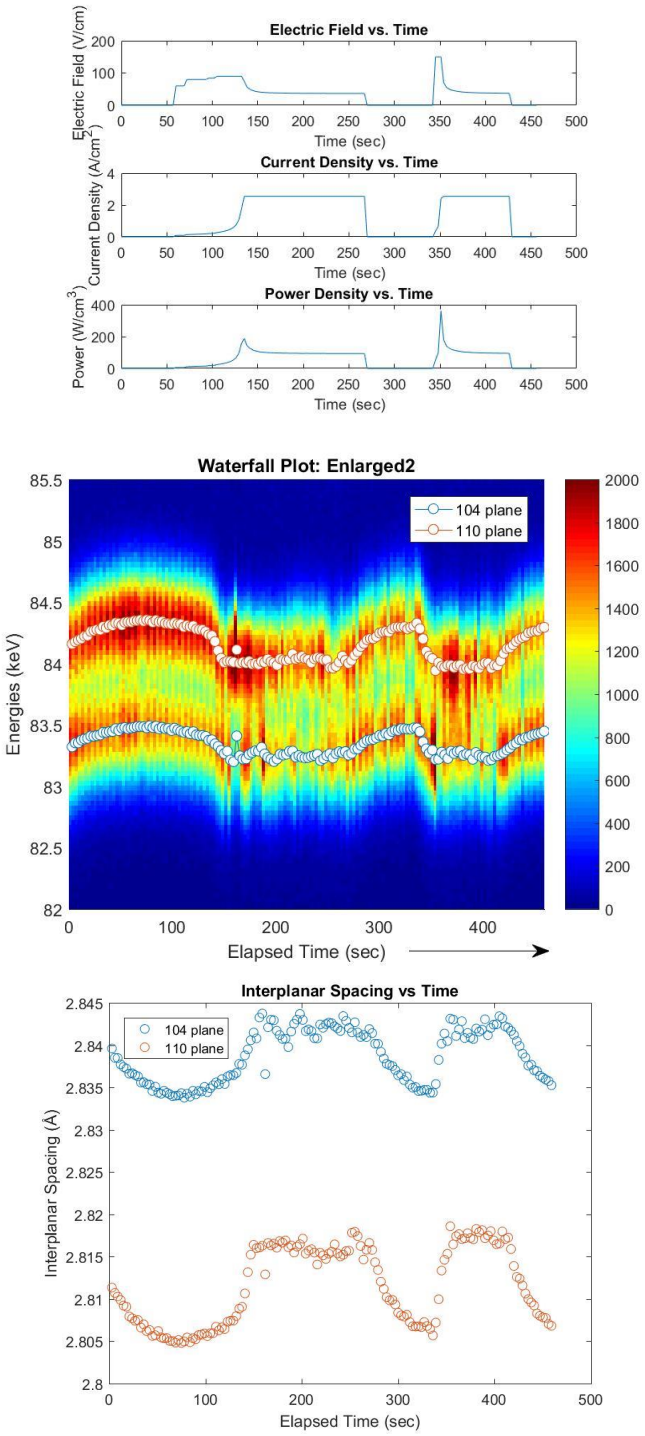

Figure 42: Electric field, current density, and power density versus time (a), peak energies versus time (b), and interplanar spacing versus time (c) for flash sintering at 350°C

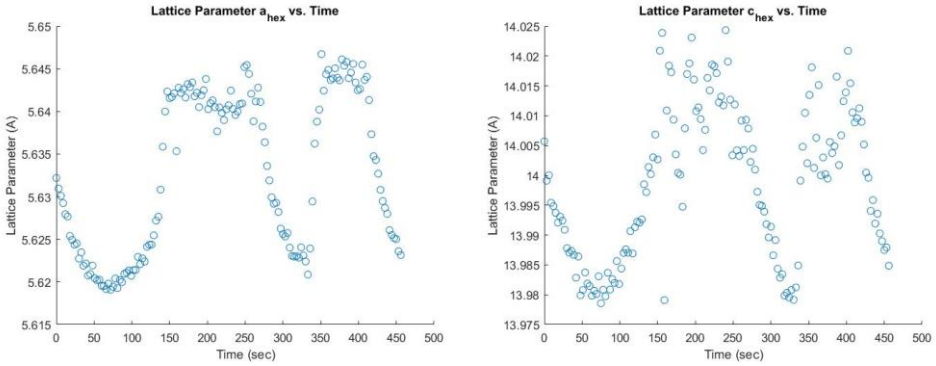

Figure 43: Change in hexagonal lattice parameters during flash

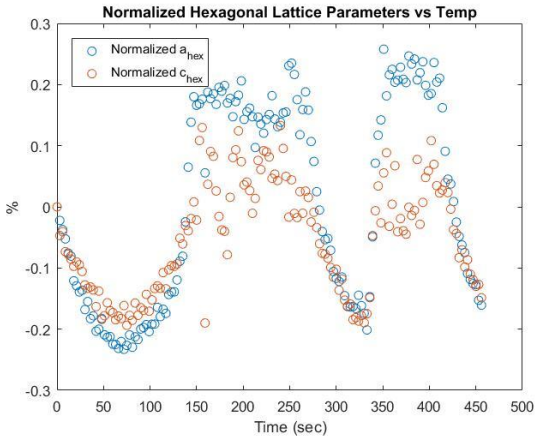

Figure 44: Normalized hexagonal lattice parameters versus time during flash at 350°C

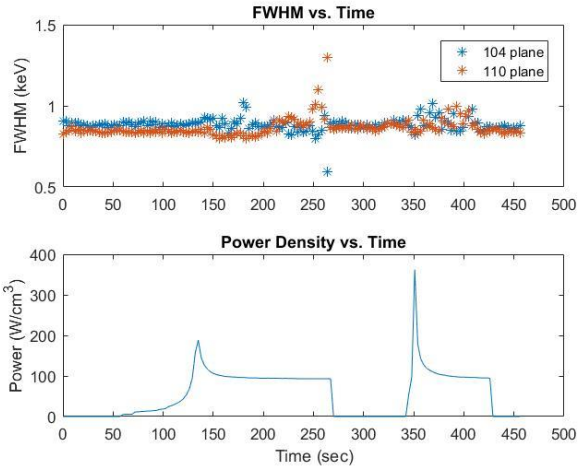

Figure 45: FWHM versus time during the flash event

Figure 46[94] shows an SEM image of densified BFO to the original milled powder. The dense BFO has low porosity but shows some grain growth compared to the 500°C sample, likely due to the relatively high electric field imposed on the sample.

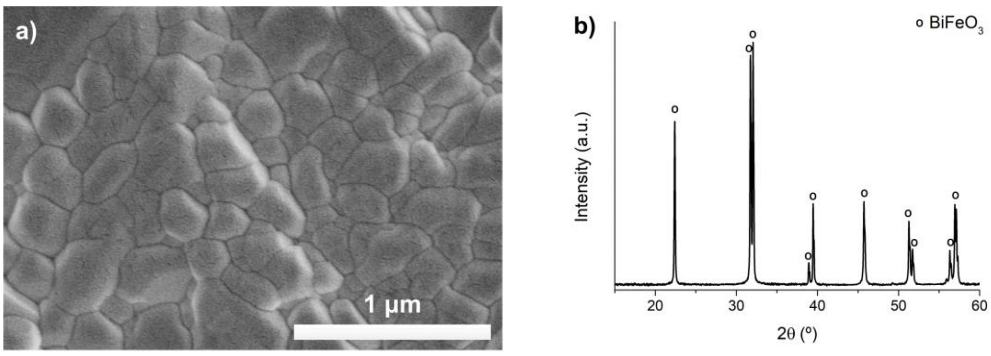

Figure 46: SEM micrograph and b) XRD pattern of the $BiFeO_3$ pellet prepared by mechanosynthesis and flash sintered at 350°C, 150 V/cm and 2.5 A/cm^2. SEM completed by Pérez-Maqueda group at CSIC-Univ. de Sevilla

5.4. Homogeneity of BFO Samples During Flash

There have been concerns that minimal information can be collected regarding the internal behavior of the sample during flash sintering, leading some to speculate that there may be some inhomogeneity in the lattice. EDXRD is a useful tool to monitor the crystal structure of the sample during flash. EDXRD spectra were taken through the thickness of a BFO green body flashed at 650°C with 25 V/cm and 2 A/cm^2. Figure 47 shows a waterfall plot of the spectra through the thickness of the sample, and it is clear that there are no anomalies within the bulk.

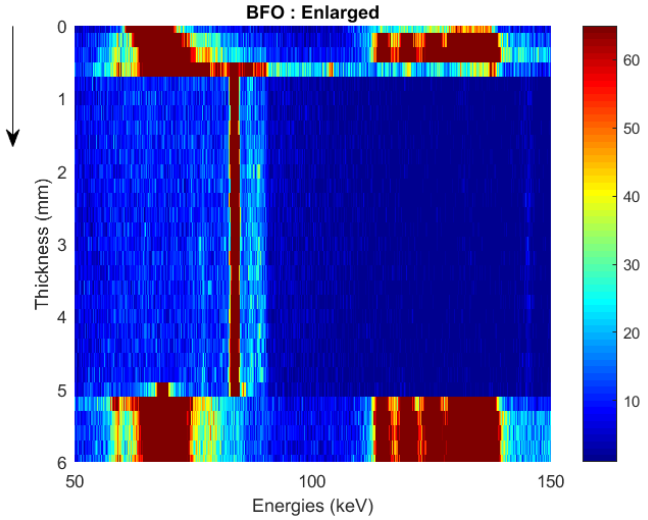

Figure 47: Waterfall plot of the thickness of a BFO sample during flash

Furthermore, SEM (see Figure 48) of a dog-bone sample prepared by the Pérez-Maqueda group and sintered at 500°C shows uniformity throughout the sample at various cross-sections.

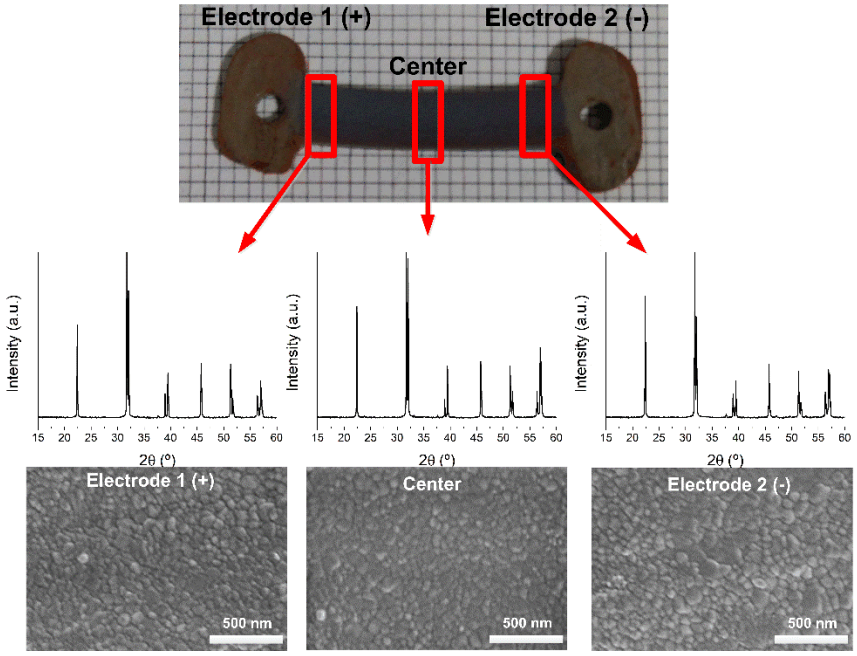

Figure 48: SEM cross-section of dogbone specimen prepared and studied by the Pérez-Maqueda group at CSIC-Univ. de Sevilla

5.5. Discussion Regarding the Anisotropy during Flash Sintering of BFO

The anisotropic behavior of the crystal lattice of bismuth ferrite during flash sintering has been consistent at 500°C and 350°C. This phenomenon is not seen during conventional temperature increases, so it's clear that the electric field has some influence over the expansion of the material.

Lebrun et al[95] recently investigated anisotropic lattice expansion during flash sintering of 3 mol% yttria stabilized tetragonal zirconia and used density functional theory to simulate the mol% of vacancy-interstitial Frenkel pairs of oxygen and zirconium. They ruled out environmental influences on the expansion since the lattice parameters change

abruptly during flash instead of an expected expansion gradient through the thickness of the sample that would have broadened their diffraction peaks.

As an oxide material, it is possible that Frenkel pairs are responsible for the similar behavior seen in the BFO experiments. This is considered further in Chapter 7.

6. ESTIMATING SAMPLE TEMPERATURE DURING FLASH SINTERING

Determining the sample temperature during flash sintering has proven to be a difficult task. Various groups have used thermocouples, pyrometers, impedance analysis, optical emission spectroscopy, and thermal expansion to estimate temperature with varying success depending on the nature of the error introduced[96].

6.1. Black Body Radiation Method

The black body radiation (BBR) model assumes that if the sample temperature is initially at the same temperature as the furnace, T_F, and is then electrically heated, the heat dissipation is equivalent to the difference in black body radiation between the sample and the furnace. The black body radiation equation for sample temperature is

$$T = T_F \left[1 + \frac{W_V}{\sigma T_F^4}\left(\frac{V}{A}\right)\right]^{1/4} \quad (11)$$

where T is the estimated sample temperature in K, T_F is the furnace temperature in K, W_V is the power density in $\mathrm{Wm^{-3}}$, σ is the Stefan-Boltzmann constant, $5.67 \times 10^{-8}\ \mathrm{Wm^{-2}K^{-4}}$, V is the volume of the sample in $\mathrm{m^3}$, and A is the surface area of the sample in $\mathrm{m^2}$. Power density was calculated based on the steady state value of the electric field during the transient stage of flash sintering. Results for each BFO experiment are shown in Table 6 and detailed calculations can be found in Appendix 1.

Table 6: Sample temperature estimates based on BBR.

Sample	Power Density (W/m^3)	Furnace Temp, T_0 (°C)	T* (°C)
Pre-Sintered BFO, Flashed at 650°C	3.97×10^7	650.76	**797.197**
Green Compact BFO, Flashed at 500°C	6.77×10^7	501.89	**806.030**
Green Compact BFO, Flashed at 350°C	1.36×10^8	356.01	**939.543**
	9.32×10^7	350.41	**837.383**
	9.42×10^7	351.17	**840.239**

Clearly, the blackbody radiation method gives values inconsistent with what we see during the experiments. The estimated temperature of the sample flashed at 650°C at 15.6V/cm and 2.55 A/cm^2 is below the Curie temperature, but we clearly saw evidence that the Curie temperature had been exceeded. Similarly, the estimated temperatures of the sample flashed at 350°C multiple times all exceed the Curie temperature, but we saw no evidence of any phase transition.

Recently, Charalambous et al[97] addressed some issues with the black body radiation method, namely that it overestimates the sample temperature by a significant degree, and suggested that using unit cell volume to estimate sample temperature provides a much more accurate value for the case of zinc oxide.

6.2. Thermal Expansion Method

Another common way of estimating temperature involves using a baseline temperature increase to compare lattice expansions during flash. Unfortunately, due to the anisotropy we see exclusively during flash, using the linear thermal expansion data is not ideal. And in fact, we see in Figure 49 that the temperature estimate for the (104) and (110) planes are quite different.

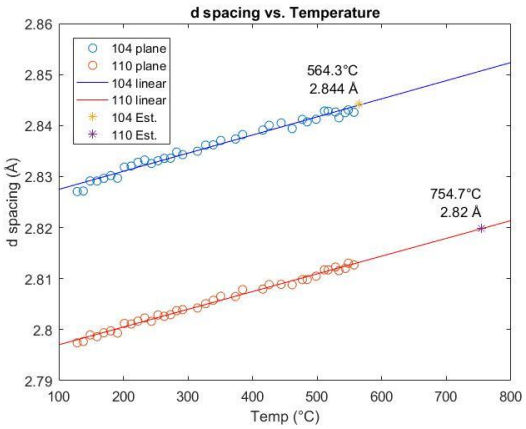

Figure 49: Sample temperature estimate during first flash at 500°C using baseline interplanar spacing data

However, as previously shown in Table 2 and Figure 5, Bucci et al[7] developed equations for the hexagonal lattice parameters and thermal expansion coefficients of BFO in terms of temperature. Using the equations in the second column of Table 2, we can calculate the temperature based on the lattice parameters during the steady state portion of the flash event. The results based on a_{hex} are shown in Table 7:

Table 7: Calculated temperatures based on a_{hex}

Flash Experiment	**Hexagonal Lattice Parameter (Å)**	**Calculated Temperature (°C)**
1st Flash, 500°C	a = 5.6494	802.3
	c = 14.0177	N/A
1st Flash, 350°C	a = 5.6448	735.0
	c = 14.0093	N/A
2nd Flash, 350°C	a = 5.6277	484.6
	c = 13.9972	N/A
3rd Flash, 350°C	a = 5.6424	699.8
	c = 14.0181	N/A

Unfortunately, the values for c_{hex} during flash are not solutions of the equation for temperature – the equation has a maximum c_{hex} of 13.9845. That said, the calculated temperatures for a_{hex} are still underestimated since these equations don't take into account the effect of the electric field.

7. DETERMINING MECHANISMS OF FLASH SINTERING OF BFO

7.1. Local Heating of Grain Boundaries

In the first flash sintering paper, Cologna et al[41] hypothesized that local heating of grain boundaries could be a mechanism of flash sintering since it leads to enhanced kinetics. Chaim et al[98] expanded on this to propose that liquid-film capillary forces could be at work in wetting the solid particles by a melt at the contact point.

Todd et al[43, 85], however, point out that densification occurs so quickly that there isn't sufficient time to sustain heating between particle contacts.

7.2. Joule Heating

Cologna et al[41] also suggested that Joule heating may be involved. In exposing the sample to an electric field, the sample temperature increases, which increases the conductivity of the sample, thereby increasing the sample temperature, and so on in a positive feedback loop.

Todd et al[43] developed an expression to account for both the furnace temperature and the electric field that would induce flashing in the case of 3 mol% yttria stabilized zirconia:

$$\Delta T_{\text{crit}} \approx \frac{RT_0^2}{Q - 5RT_0} \qquad (12)$$

where R is the gas constant, 8.314 $\text{Jmol}^{-1}\text{K}^{-1}$, T_0 is the furnace temperature in Kelvin, and Q is the activation energy, 1.15 eV for BFO[18].

Hewitt et al[99] developed a theoretical model for Joule heating during flash sintering. Their model ignored any material changes due to sintering and assumed an axisymmetric sample (see Figure 50).

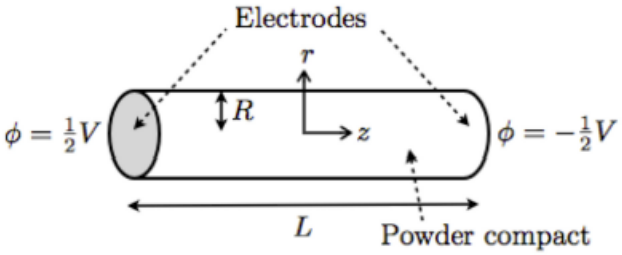

Figure 50: Model of cylindrical sample

The model assumes that the thermal conductivity of the sample is counteracted by cooling from the sides of the sample via radiation, conduction, and convection and cooling from the ends at the locations of the electrodes.

There is a lot of uncertainty in this method when applied to BFO due varying reports of thermal and electrical conductivity, Arrhenius rate factor, and activation energy. That said, the strength of Joule heating, λ, in this model is found to be:

$$\lambda = \frac{\sigma_0 V_0^2 R^2}{k \Delta T L^2} \quad (13)$$

where σ_0 is the conductivity at the furnace temperature, V_0 is the applied voltage to the sample, R is the sample radius, k is the thermal conductivity of the sample, ΔT is the change in temperature, and L is the thickness of the sample. Special cases were also developed depending on whether the electrodes are thermally insulating, the sides are weakly cooled, the heating and cooling rates are small, and the sample has a high aspect ratio.

7.3. Nucleation of Avalanche of Frenkel Defects

Cologna et al[41] also proposed that the electric field could be conducive to an avalanche of Frenkel defects. These defects would increase the rate of diffusion through the sample. Figure 51[100] shows a Frenkel pair:

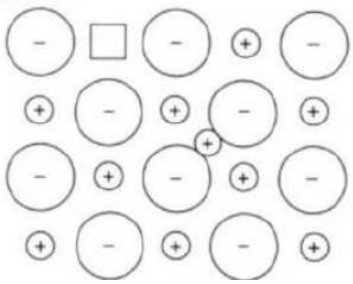

Figure 51: Frenkel pair, where the vacancy is denoted by the square

Naik et al[42] developed a model that analyzes nucleation of the non-linear transition from an insulating to a conducting state of the sample. They hypothesize that an embryo of high dielectric constant and just a few nanometers in diameter, assumed to arise from aggregation of aligned dipoles made of vacancy-interstitial Frenkel pairs, is formed under the influence of an electric field. The driving force for nucleation is from the polarization energy of this aggregate per unit volume, ΔG_V, given by Equation (14):

$$\Delta G_V = \frac{1}{2}\varepsilon_0 \varepsilon_E E_j^2 \quad (14)$$

where ε_0 is the permittivity of the vacuum, ε_E is the dielectric constant of the embryo, and E_J is the applied electric field. The total free energy, ΔG, is the difference between the polarization energy and the energy of the interface, γ_E, that it forms with the parent lattice:

$$\Delta G = -4\pi r^3 \, \Delta G_V + 4\pi r^2 \gamma_E \quad (15)$$

where r is the radius of the embryo. The total free energy is maximized when a critical radius is reached, $r*$, which is denoted by Equations (16) and (17):

$$\Delta G* = \frac{1}{2}\left(\frac{4\pi}{3}r*^3\right)\Delta G_V \quad (16)$$

$$r* = \frac{4\gamma_E}{\varepsilon_0 \varepsilon_E E_j^2} \quad (17)$$

Naik et al also calculated the probability of nucleation as a function of interfacial energy, assuming a reasonable value of interface energy of $\gamma_E = 1$ mJ m^{-1}, as shown in Figure 52[42]:

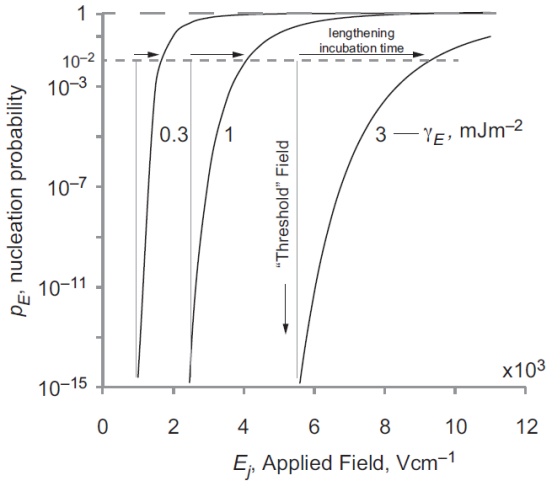

Figure 52: Probability of nucleation of an embryo based on interfacial energy, based on a dielectric constant of approximately 10^6

Narayan[101] developed a model for grain growth during flash sintering of materials and specified that grain growth can be inhibited as a result of vacancy segregation.

7.4. Qualifying the Mechanisms with Application to BFO

It is this lab's opinion that, based on the anisotropic behavior of the lattice expansion during flash sintering, the nucleation of an avalanche of Frenkel defects is a likely mechanism for flash sintering. That isn't to say that Joule heating doesn't contribute at all, but the exact nature of the coupling remains ambiguous.

8. CONCLUSION AND FUTURE WORK

The feasibility of flash sintering bismuth ferrite was studied. The experiments detailed in this thesis used energy dispersive X-ray diffraction (EDXRD) to elucidate what happens to the sample structure during flash. Different constant electric fields were applied to both pre-sintered samples and green bodies at furnace temperatures significantly below the Curie temperature of BFO. Densification is comparable to samples sintered by conventional methods. Unlike conventional sintering methods, anisotropic behavior was observed during lattice expansion upon exposure to the electric field that is inconsistent with simple heating. Grain growth increased as the samples were sintered for longer times, but first flash experiments showed minimal grain growth in the samples. During flash, samples were found to be structurally consistent within the bulk. Estimating sample temperature still remains elusive due to the anisotropic nature of the lattice expansion, but calculations do provide some idea about the temperature the samples experience during flash. While Joule heating cannot be eliminated as a possibility, it appears that nucleation of avalanches of Frenkel defects is a likely explanation for the anisotropy during flash.

There are several directions this research could proceed. First, there is certainly a need for modeling of this setup. It is of immediate importance to implement density functional theory to estimate the number of Frenkel pairs being formed during flash sintering of BFO. In this way, we can begin to quantify the anisotropic behavior. Additionally, developing a three-dimensional model of the flash sintering furnace being used in our laboratory can also elucidate information regarding sample shrinkage and temperature gradient. For this, COMSOL™ Multiphysics is a useful tool that can

incorporate the thermal, electrical, and mechanical phenomena simultaneously for a more accurate simulation.

Since flash sintering is still relatively new, there is also more room for experimental work as well. Certainly more work can be done to improve temperature estimates during flash sintering. Additionally, some studies have been done on dopants for BFO[37, 102, 103, 104, 105, 106, 107], but nothing comprehensive has been pursued in flashing doped BFO. It is also of interest to study flash sintering of bismuth ferrite-based composites[108, 109, 110, 111, 112]. While bismuth ferrite has an advantage of having a high Curie temperature, other perovskite-type ferrites, such as gadolinium orthoferrite, may be of interest to flash sinter as well since they can exhibit electrical and magnetic properties as well. The difficulty with this is developing the initial powders for some of these materials since they, too, can be challenging to make.

APPENDIX 1

This table, created in Excel, was used to calculate black body radiation values.

Stage	Sample #	Regular Scan #	Steady State Current (A)	Steady State Current Density (A/m^2)	Steady State Voltage (V)	Steady State Electric Field (V/m)	Power Density (W/m^3)	Furnace Temp, T_F (°C)	Furnace Temp, T_F (K)	T* (°C)
III	1	2	0.5	2.55E+04	7.8	1560	3.97E+07	650.76	923.91	797.197
III	1	3	1	5.09E+04	7.2	1440	7.33E+07	654.38	927.53	888.029
III	3	1	0.5	2.55E+04	13.3	2660	6.77E+07	501.89	775.04	806.030
III	3	5	0.5	2.55E+04	12.4	2480	6.32E+07	504.63	777.78	793.431
III	3	5	0.25	1.27E+04	17.3	3460	4.41E+07	504.74	777.89	730.241
III	5	1	0.5	2.55E+04	26.8	5360	1.36E+08	356.01	629.16	939.543
III	5	2	0.5	2.55E+04	18.3	3660	9.32E+07	350.41	623.56	837.383
III	5	2	0.5	2.55E+04	18.5	3700	9.42E+07	351.17	624.32	840.239

emissivity	1	
sigma	5.67E-08	W/m^2K^2
thickness	0.005	m
diameter	0.005	m
perimeter	0.015707963	m

area	1.9635E-05	m^2
volume	9.81748E-08	m^3
surf area	0.00011781	m^2
Vol/Surf	0.000833333	m

APPENDIX 2

Additional studies on sintering ferrite materials were attempted but unsuccessful. Cobalt ferrite and nickel ferrite are both spinel-type ferrites but for both materials, the current channeled through the samples and did not densify. A composite of spinel-type zinc ferrite and bismuth ferrite was also studied with the aim of determining the threshold of zinc ferrite for an improvement of material properties. However, the amount of zinc ferrite required for flash was so little that the X-ray beam was attenuated enough so as not to pick up any traces of it to monitor.

REFERENCES

1. J. R. Teague, R. Gerson, and W. J. James, "Dielectric Hysteresis in Single Crystal BiFeO3," *Solid State Communications,* 8[13] 1073-74 (1970).
2. I. Sosnowska, T. Peterlin-Neumaier, and E. Steichele, "Spiral magnetc ordering in bismuth ferrite," *Journal of Physics C: Solid State Physics,* 15 4835-46 (1982).
3. G. Catalan and J. F. Scott, "Physics and Applications of Bismuth Ferrite," *Advanced Materials,* 21[24] 2463-85 (2009).
4. P. Fischer, M. Polomska, I. Sosnowska, and M. Szymanski, "Temperature dependence of the crystal and magnetic structures of BiFeO3," *Journal of Physics C: Solid State Physics,* 13 1934-40 (1980).
5. B. D. Cullity, "Elements of X-Ray Diffraction,″ pp. 514 Vol. 1. Addison-Wesley: Reading, Massachusetts, (1956).
6. J. G. Wu, Z. Fan, D. Q. Xiao, J. G. Zhu, and J. Wang, "Multiferroic bismuth ferrite-based materials for multifunctional applications: Ceramic bulks, thin films and nanostructures," *Progress in Materials Science,* 84 335-402 (2016).
7. J. D. Bucci, B. K. Robertson, and W. J. James, "The Precision Determination of the Lattice Parameters and the Coefficients of Thermal Expansion of BiFeO3," *Journal of Applied Crystallography,* 5 187-91 (1972).
8. F. Kubel and H. Schmid, "Structure of a Ferroelectric and Ferroelastic Monodomain Crystal of the Perovskite BiFeO3," *Acta Crystallogr B,* B46 698-702 (1990).
9. A. M. Kadomtseva, Y. F. Popov, A. P. Pyatakov, G. P. Vorob'ev, A. K. Zvezdin, and D. Viehland, "Phase transitions in multiferroic BiFeO3 crystals, thin-layers, and ceramics: enduring potential for a single phase, room-temperature magnetoelectric 'holy grail'," *Phase Transitions,* 79[12] 1019-42 (2006).
10. D. C. Arnold, K. S. Knight, F. D. Morrison, and P. Lightfoot, "Ferroelectric-Paraelectric Transition in BiFeO3: Crystal Structure of the Orthorhombic beta Phase," *Physical Review Letters,* 102[2] 027602 (2009).
11. A. Perejón, P. E. Sánchez-Jiménez, J. M. Criado, and L. A. Pérez-Maqueda, "Thermal Stability of Multiferroic BiFeO3: Kinetic Nature of the β–γ Transition and Peritectic Decomposition," *The Journal of Physical Chemistry C,* 118[45] 26387-95 (2014).
12. A. N. Morozovska, V. V. Khist, M. D. Glinchuk, V. Gopalan, and E. A. Eliseev, "Linear antiferrodistortive-antiferromagnetic effect in multiferroics: Physical manifestations," *Physical Review B,* 92[5] 054421 (2015).
13. X.-S. Cao, "Anomalous Specific Heat of Multiferroic BiFeO3," *Journal of Low Temperature Physics* (2017).
14. M. S. Bernardo, "Synthesis, microstructure and properties of BiFeO3-based multiferroic materials: A review," *Boletín de la Sociedad Española de Cerámica y Vidrio,* 53[1] 1-14 (2014).
15. T. Rojac, M. Makarovic, J. Walker, H. Ursic, D. Damjanovic, and T. Kos, "Piezoelectric response of BiFeO3 ceramics at elevated temperatures," *Applied Physics Letters,* 109[4] 042904 (2016).
16. M. H. Basiri, H. Shokrollahi, and G. Isapour, "Effects of La content on the magnetic, electric and structural properties of BiFeO3," *Journal of Magnetism and Magnetic Materials,* 354 184-89 (2014).

17. S. Chaturvedi, M. M. Shirolkar, R. Rajendra, S. Singh, N. Ballav, and S. Kulkarni, "Coercivity and exchange bias of bismuth ferrite nanoparticles isolated by polymer coating," *Journal of Applied Physics*, 115[12] 123906 (2014).
18. A. Perejon, N. Maso, A. R. West, P. E. Sanchez-Jimenez, R. Poyato, J. M. Criado, and L. A. Perez-Maqueda, "Electrical Properties of Stoichiometric BiFeO3 Prepared by Mechanosynthesis with Either Conventional or Spark Plasma Sintering," *Journal of the American Ceramic Society*, 96[4] 1220-27 (2013).
19. H. Y. Dai, Z. P. Chen, T. Li, R. Z. Xue, and J. Chen, "Structural and Electrical Properties of Bismuth Ferrite Ceramics Sintered in Different Atmospheres," *Journal of Superconductivity and Novel Magnetism*, 26[10] 3125-32 (2013).
20. M. Schrade, N. Maso, A. Perejon, L. A. Perez-Maqueda, and A. R. West, "Defect chemistry and electrical properties of BiFeO3," *Journal of Materials Chemistry C*, 5[38] 10077-86 (2017).
21. C. Fu, X. Long, W. Cai, G. Chen, and X. Deng, "Effect of Sintering Temperature on the Microstructures and Ferroelectric Properties of Bismuth Ferrite Ceramics," *Ferroelectrics*, 445[1] 114-20 (2013).
22. C. R. Bowen, H. A. Kim, P. M. Weaver, and S. Dunn, "Piezoelectric and ferroelectric materials and structures for energy harvesting applications," *Energy Environ. Sci.*, 7[1] 25-44 (2014).
23. E. Heifets, E. A. Kotomin, A. A. Bagaturyants, and J. Maier, "Ab Initio Study of BiFeO3: Thermodynamic Stability Conditions," *The Journal of Physical Chemistry Letters*, 6[14] 2847-51 (2015).
24. C. Tablero, "An evaluation of BiFeO3 as a photovoltaic material," *Solar Energy Materials and Solar Cells*, 171 161-65 (2017).
25. T. Gao, Z. Chen, Q. Huang, F. Niu, X. Huang, L. Qin, and Y. Huang, "A Review: Preparation of Bismuth Ferrite Nanoparticles and its Applications in Visible-Light Induced Photocatalyses," *Review of Advanced Material Science*, 40 97-109 (2015).
26. M. Dziubaniuk, R. Bujakiewicz-Koronska, J. Suchanicz, J. Wyrwa, and M. Rekas, "Application of bismuth ferrite protonic conductor for ammonia gas detection," *Sensors and Actuators B: Chemical*, 188 957-64 (2013).
27. H. Wu, J. Zhou, L. Liang, L. Li, and X. Zhu, "Fabrication, Characterization, Properties, and Applications of Low-Dimensional BiFeO3Nanostructures," *Journal of Nanomaterials*, 2014 1-14 (2014).
28. C. E. J. Dancer, "Flash sintering of ceramic materials," *Materials Research Express*, 3[10] 102001 (2016).
29. C. Ricardo and B. Klaus Van, "Sintering: Mechanisms of Convention Nanodensification and Field Assisted Processes," Vol. 35. Springer Berlin Heidelberg: Berlin, Heidelberg, (2013).
30. X. L. Deng, X. B. Liu, W. Cai, C. L. Fu, and J. M. Huang, "The Influence of Sintering Temperature on the Microstructure and Electrical Properties of BiFeO3 Ceramics," *Key Engineering Materials*, 602-603 942-46 (2014).
31. A. Sagdeo, P. Mondal, A. Upadhyay, A. K. Sinha, A. K. Srivastava, S. M. Gupta, P. Chowdhury, T. Ganguli, and S. K. Deb, "Correlation of microstructural and physical properties in bulk BiFeO3 prepared by rapid liquid-phase sintering," *Solid State Sciences*, 18 1-9 (2013).

32. C. Ponzoni, M. Cannio, R. Rosa, T. Chudoba, E. Pietrzykowka, V. Buscaglia, E. Finocchio, P. Nanni, W. Łojkowski, and C. Leonelli, "Effect of low-temperature high-pressure sintering on BiFeO3 density, electrical magnetic and structural properties," *Phase Transitions,* 86[11] 1104-14 (2013).
33. C. Fu, X. Long, W. Cai, G. Chen, and X. Deng, "Microstructures and dielectric properties of bismuth ferrite ceramics prepared using two sintering methods," *Journal of Ceramic Processing Research,* 15[5] 305-07 (2014).
34. K. R. Obulesu and K. C. J. Raju, "Effect of conventional and microwave sintering on ceramic BiFeO3," 1228-29 (2013).
35. W. Cai, C. Fu, W. Hu, G. Chen, and X. Deng, "Effects of microwave sintering power on microstructure, dielectric, ferroelectric and magnetic properties of bismuth ferrite ceramics," *Journal of Alloys and Compounds,* 554 64-71 (2013).
36. A. Perejón, N. Masó, A. R. West, P. E. Sánchez-Jiménez, R. Poyato, J. M. Criado, L. A. Pérez-Maqueda, and D. Viehland, "Electrical Properties of Stoichiometric BiFeO3Prepared by Mechanosynthesis with Either Conventional or Spark Plasma Sintering," *Journal of the American Ceramic Society,* 96[4] 1220-27 (2013).
37. A. Perejón, P. E. Sánchez-Jiménez, R. Poyato, N. Masó, A. R. West, J. M. Criado, and L. A. Pérez-Maqueda, "Preparation of phase pure, dense fine grained ceramics by conventional and spark plasma sintering of La-substituted BiFeO3 nanoparticles," *Journal of the European Ceramic Society,* 35[8] 2283-93 (2015).
38. L. C. Wang, Z. H. Wang, S. L. He, X. Li, P. T. Lin, J. R. Sun, and B. G. Shen, "Enhanced magnetization and suppressed current leakage in BiFeO3 ceramics prepared by spark plasma sintering of sol–gel derived nanoparticles," *Physica B: Condensed Matter,* 407[8] 1196-202 (2012).
39. R. A. M. Gotardo, D. Montanher, O. A. Protzek, L. F. Cotica, I. A. Santos, D. S. F. Viana, W. J. Nascimento, D. Garcia, and J. A. Eiras, "Multiferroic Properties and Piezoelectric Characterizations of Bismuth Ferrite Based Compounds Produced by Spark Plasma Sintering," *Advanced Materials Research,* 975 257-62 (2014).
40. Z. Dai and Y. Akishige, "Electrical properties of BiFeO3–BaTiO3 ceramics fabricated by mechanochemical synthesis and spark plasma sintering," *Materials Letters,* 88 36-39 (2012).
41. M. Cologna, B. Rashkova, and R. Raj, "Flash Sintering of Nanograin Zirconia in <5 s at 850°C," *Journal of the American Ceramic Society,* 93[11] 3556-59 (2010).
42. K. S. Naik, V. M. Sglavo, and R. Raj, "Flash sintering as a nucleation phenomenon and a model thereof," *Journal of the European Ceramic Society,* 34[15] 4063-67 (2014).
43. R. I. Todd, E. Zapata-Solvas, R. S. Bonilla, T. Sneddon, and P. R. Wilshaw, "Electrical characteristics of flash sintering: thermal runaway of Joule heating," *Journal of the European Ceramic Society,* 35[6] 1865-77 (2015).
44. R. Raj, "Analysis of the Power Density at the Onset of Flash Sintering," *Journal of the American Ceramic Society* (2016).
45. M. Cologna, J. S. C. Francis, and R. Raj, "Field assisted and flash sintering of alumina and its relationship to conductivity and MgO-doping," *Journal of the European Ceramic Society,* 31[15] 2827-37 (2011).

46. M. Biesuz and V. M. Sglavo, "Flash sintering of alumina: Effect of different operating conditions on densification," *Journal of the European Ceramic Society,* 36[10] 2535-42 (2016).
47. N. Shomrat, S. Baltianski, C. A. Randall, and Y. Tsur, "Flash sintering of potassium-niobate," *Journal of the European Ceramic Society,* 35[7] 2209-13 (2015).
48. E. Bichaud, J. M. Chaix, C. Carry, M. Kleitz, and M. C. Steil, "Flash sintering incubation in Al2O3/TZP composites," *Journal of the European Ceramic Society,* 35[9] 2587-92 (2015).
49. E. Zapata-Solvas, S. Bonilla, P. R. Wilshaw, and R. I. Todd, "Preliminary investigation of flash sintering of SiC," *Journal of the European Ceramic Society,* 33[13-14] 2811-16 (2013).
50. E. Olevsky, S. M. Rolfing, and A. Maximenko, "Flash (Ultra-Rapid) Spark-Plasma Sintering of Silicon Carbide," *Scientific Reports,* 6 33408 (2016).
51. S. K. Jha, J. M. Lebrun, and R. Raj, "Phase transformation in the alumina–titania system during flash sintering experiments," *Journal of the European Ceramic Society,* 36[3] 733-39 (2016).
52. N. Shomrat, S. Baltianski, E. Dor, and Y. Tsur, "The influence of doping on flash sintering conditions in SrTi1-xFexO3-delta," *Journal of the European Ceramic Society,* 37[1] 179-88 (2017).
53. K. S. Naik, V. M. Sglavo, and R. Raj, "Field assisted sintering of ceramic constituted by alumina and yttria stabilized zirconia," *Journal of the European Ceramic Society,* 34[10] 2435-42 (2014).
54. A. Karakuscu, M. Cologna, D. Yarotski, J. Won, J. S. C. Francis, R. Raj, B. P. Uberuaga, and P. Davies, "Defect Structure of Flash-Sintered Strontium Titanate," *Journal of the American Ceramic Society,* 95[8] 2531-36 (2012).
55. F. Lemke, W. Rheinheimer, and M. J. Hoffmann, "A comparison of power controlled flash sintering and conventional sintering of strontium titanate," *Scripta Materialia,* 130 187-90 (2017).
56. J.-C. M'Peko, J. S. C. Francis, and R. Raj, "Field-assisted sintering of undoped BaTiO3: Microstructure evolution and dielectric permittivity," *Journal of the European Ceramic Society,* 34[15] 3655-60 (2014).
57. J. C. M'Peko, J. S. C. Francis, and R. Raj, "Field-assisted sintering of undoped BaTiO3: Microstructure evolution and dielectric permittivity," *Journal of the European Ceramic Society,* 34[15] 3655-60 (2014).
58. R. Muccillo and E. N. S. Muccillo, "Electric field-assisted flash sintering of tin dioxide," *Journal of the European Ceramic Society,* 34[4] 915-23 (2014).
59. L. M. Jesus, R. S. Silva, R. Raj, and J. C. M'Peko, "Electric field-assisted flash sintering of CaCu3Ti4O12: Microstructure characteristics and dielectric properties," *Journal of Alloys and Compounds,* 682 753-58 (2016).
60. S. K. Jha, R. Raj, and I. W. Chen, "The Effect of Electric Field on Sintering and Electrical Conductivity of Titania," *Journal of the American Ceramic Society,* 97[2] 527-34 (2014).
61. S. K. Jha, J. M. Lebrun, K. C. Seymour, W. M. Kriven, and R. Raj, "Electric field induced texture in titania during experiments related to flash sintering," *Journal of the European Ceramic Society,* 36[1] 257-61 (2016).

62. Y. Y. Zhang, J. Y. Nie, and J. Luo, "Effects of phase and doping on flash sintering of TiO2," *J. Ceram. Soc. Jpn.,* 124[4] 296-300 (2016).
63. X. Hao, Y. Liu, Z. Wang, J. Qiao, and K. Sun, "A novel sintering method to obtain fully dense gadolinia doped ceria by applying a direct current," *Journal of Power Sources,* 210 86-91 (2012).
64. T. Jiang, Z. Wang, J. Zhang, X. Hao, D. Rooney, Y. Liu, W. Sun, J. Qiao, K. Sun, and R. Hay, "Understanding the Flash Sintering of Rare-Earth-Doped Ceria for Solid Oxide Fuel Cell," *Journal of the American Ceramic Society,* 98[6] 1717-23 (2015).
65. M. Biesuz, G. Dell'Agli, L. Spiridigliozzi, C. Ferone, and V. M. Sglavo, "Conventional and field-assisted sintering of nanosized Gd-doped ceria synthesized by co-precipitation," *Ceramics International,* 42[10] 11766-71 (2016).
66. F. Maglia, F. Farina, M. Dapiaggi, I. G. Tredici, and U. Anselmi-Tamburini, "Transport properties in bulk nanocrystalline Sm-doped ceria with doping content between 2 and 30at.%," *Solid State Ionics,* 225 412-15 (2012).
67. L. Spiridigliozzi, M. Biesuz, G. Dell'Agli, E. Di Bartolomeo, F. Zurlo, and V. M. Sglavo, "Microstructural and electrical investigation of flash-sintered Gd/Sm-doped ceria," *Journal of Materials Science,* 52[12] 7479-88 (2017).
68. H. Yoshida, Y. Sakka, T. Yamamoto, J.-M. Lebrun, and R. Raj, "Densification behaviour and microstructural development in undoped yttria prepared by flash-sintering," *Journal of the European Ceramic Society,* 34[4] 991-1000 (2014).
69. H. Yoshida, K. Morita, B.-N. Kim, Y. Sakka, and T. Yamamoto, "Reduction in sintering temperature for flash-sintering of yttria by nickel cation-doping," *Acta Materialia,* 106 344-52 (2016).
70. H. Yoshida, Y. Sakka, T. Yamamoto, J. M. Lebrun, and R. Raj, "Field–assisted and flash sintering of nanocrystalline yttria: Densification and microstructural evolution," in Electric Field Assisted Sintering and Related Phenomena Far From Equilibrium.
71. A. L. G. Prette, M. Cologna, V. Sglavo, and R. Raj, "Flash-sintering of Co2MnO4 spinel for solid oxide fuel cell applications," *Journal of Power Sources,* 196[4] 2061-65 (2011).
72. M. Cologna, A. L. G. Prette, and R. Raj, "Flash-Sintering of Cubic Yttria-Stabilized Zirconia at 750°C for Possible Use in SOFC Manufacturing," *Journal of the American Ceramic Society,* 94[2] 316-19 (2011).
73. E. K. Akdoğan, I. Savkliyidiz, H. Bicer, W. A. Paxton, F. Toksoy, Z. Zhong, and T. Tsakalakos, "Anomalous lattice expansion in yttria stabilized zirconia under simultaneous applied electric and thermal fields: A time-resolved in situ energy dispersive x-ray diffractometry study with an ultrahigh energy synchrotron probe," *Journal of Applied Physics,* 113 233503 (2013).
74. J. C. M'Peko, J. S. C. Francis, R. Raj, and D. Lupascu, "Impedance Spectroscopy and Dielectric Properties of Flash Versus Conventionally Sintered Yttria-Doped Zirconia Electroceramics Viewed at the Microstructural Level," *Journal of the American Ceramic Society,* 96[12] 3760-67 (2013).
75. J. G. Pereira da Silva, J.-M. Lebrun, H. A. Al-Qureshi, R. Janssen, R. Raj, and E. Olevsky, "Temperature Distributions During Flash Sintering of 8% Yttria-Stabilized Zirconia," *Journal of the American Ceramic Society,* 98[11] 3525-28 (2015).

76. A. Gaur and V. M. Sglavo, "Densification of La0.6Sr0.4Co0.2Fe0.8O3 ceramic by flash sintering at temperature less than 100 °C," *Journal of Materials Science*, 49[18] 6321-32 (2014).
77. F. H. Teherani, D. C. Look, D. J. Rogers, B. Dargatz, J. Gonzalez-Julian, and O. Guillon, "Effect of electric field and atmosphere on the processing of nanocrystalline ZnO," 8987 89871H (2014).
78. Y. Zhang, J.-I. Jung, and J. Luo, "Thermal runaway, flash sintering and asymmetrical microstructural development of ZnO and ZnO–Bi2O3 under direct currents," *Acta Materialia*, 94 87-100 (2015).
79. J. Langer, M. J. Hoffmann, and O. Guillon, "Electric Field-Assisted Sintering and Hot Pressing of Semiconductive Zinc Oxide: A Comparative Study," *Journal of the American Ceramic Society*, 94[8] 2344-53 (2011).
80. C. Schmerbauch, J. Gonzalez-Julian, R. Röder, C. Ronning, O. Guillon, and L. Gauckler, "Flash Sintering of Nanocrystalline Zinc Oxide and its Influence on Microstructure and Defect Formation," *Journal of the American Ceramic Society*, 97[6] 1728-35 (2014).
81. H. Yoshida, P. Biswas, R. Johnson, and M. K. Mohan, "Flash-sintering of magnesium aluminate spinel (MgAl2O4) ceramics," *Journal of the American Ceramic Society*, 100[2] 554-62 (2017).
82. S. Grasso, Y. Sakka, N. Rendtorff, C. Hu, G. Maizza, H. Borodianska, and O. Vasylkiv, "Modeling of the temperature distribution of flash sintered zirconia," *J. Ceram. Soc. Jpn.*, 119[2] 144-46 (2011).
83. J. A. Downs, V. M. Sglavo, and R. Raj, "Electric Field Assisted Sintering of Cubic Zirconia at 390°C," *Journal of the American Ceramic Society*, 96[5] 1342-44 (2013).
84. A. Gaur and V. M. Sglavo, "Flash-sintering of MnCo2O4 and its relation to phase stability," *Journal of the European Ceramic Society*, 34[10] 2391-400 (2014).
85. R. I. Todd, "Flash Sintering of Ceramics: A Short Review," pp. 1-12. in Proceedings of the IV Advanced Ceramics and Applications Conference**.** Edited by B. Lee, R. Gadow, and V. Mitic. Atlantis Press, Paris, 2017.
86. L. A. Perez-Maqueda, E. Gil-Gonzalez, A. Perejon, J.-M. Lebrun, P. E. Sanchez-Jimenez, and R. Raj, "Flash Sintering of highly insulating nanostructured phase-pure BiFeO3," *Journal of the American Ceramic Society*, 100[8] 3365–69 (2017).
87. E. Gil-Gonzalez, A. Perejon, P. E. Sanchez-Jimenez, M. J. Sayagues, R. Raj, and L. A. Perez-Maqueda, "Phase-pure BiFeO3 produced by reaction flash-sintering of Bi2O3 and Fe2O3," *Journal of Materials Chemistry A* (2018).
88. S. Jauhar, J. Kaur, A. Goyal, and S. Singhal, "Tuning the properties of cobalt ferrite: a road towards diverse applications," *Rsc Advances*, 6[100] 97694-719 (2016).
89. A. Perejón, N. Murafa, P. E. Sánchez-Jiménez, J. M. Criado, J. Subrt, M. J. Diánez, and L. A. Pérez-Maqueda, "Direct mechanosynthesis of pure BiFeO3 perovskite nanoparticles: reaction mechanism," *Journal of Materials Chemistry C*, 1[22] 3551 (2013).
90. I. Sosnowska, R. Przeniosło, P. Fischer, and V. A. Murashov, "Neutron diffraction studies of the crystal and magnetic structures of BiFeO3 and Bi0.93La0.07FeO3," *Journal of Magnetism and Magnetic Materials*, 160 384-85 (1996).

91. M. Wojdyr, "Fityk: a general-purpose peak fitting program," *Journal of Applied Crystallography,* 43[5 Part 1] 1126-28 (2010).
92. J. M. Lebrun, K. Jha Shikhar, J. McCormack Scott, M. Kriven Waltraud, and R. Raj, "Broadening of Diffraction Peak Widths and Temperature Nonuniformity During Flash Experiments," *Journal of the American Ceramic Society,* 99[10] 3429-34 (2016).
93. J. M. Lebrun, S. K. Jha, and R. Raj, "The Change of X-ray Diffraction Peak Width During in situ Conventional Sintering of Nanoscale Powders," *Journal of the American Ceramic Society,* 99[3] 1-4 (2016).
94. L. A. Perez-Maqueda, E. Gil-Gonzalez, M. A. Wassel, S. K. Jha, A. Perejon, H. Charalambous, J. Okasinski, P. E. Sanchez-Jimenez, and T. Tsakalakos, "Insight into the BiFeO3 flash sintering process by in-situ energy dispersive X-ray diffraction," *Ceramics International* (Accepted 2018).
95. J. M. Lebrun, C. S. Hellberg, S. K. Jha, W. M. Kriven, A. Steveson, K. C. Seymour, N. Bernstein, S. C. Erwin, and R. Raj, "In-situ measurements of lattice expansion related to defect generation during flash sintering," *Journal of the American Ceramic Society* n/a-n/a (2017).
96. M. Yu, S. Grasso, R. McKinnon, T. Saunders, and M. J. Reece, "Review of flash sintering: materials, mechanisms and modelling," *Advances in Applied Ceramics,* 116[1] 24-60 (2017).
97. H. Charalambous, S. K. Jha, R. T. Lay, A. Cabales, J. Okasinski, and T. Tsakalakos, "Investigation of temperature approximation methods during flash sintering of ZnO," *Ceramics International* (2018).
98. R. Chaim, "Liquid Film Capillary Mechanism for Densification of Ceramic Powders during Flash Sintering," *Materials,* 9[4] (2016).
99. I. J. Hewitt, A. A. Lacey, and R. I. Todd, "A Mathematical Model for Flash Sintering," *Mathematical Modelling of Natural Phenomena,* 10[6] 77-89 (2015).
100. M. Ohring, "Engineering materials science.″ Academic Press: San Diego, (1995).
101. J. Narayan, "Grain growth model for electric field-assisted processing and flash sintering of materials," *Scripta Materialia,* 68[10] 785-88 (2013).
102. M. K. Mishra and R. N. Mahaling, "Single or both site doped BiFeO3 - Which is better candidate for profound electronic device applications?," *Chinese Journal of Physics* (2018).
103. L. Chen, L. Zheng, Y. He, J. Zhang, Z. Mao, and X. Chen, "The local distortion and electronic behavior in Mn doped BiFeO3," *Journal of Alloys and Compounds,* 633 216-19 (2015).
104. Q.-Y. Rong, W.-Z. Xiao, G. Xiao, A.-M. Hu, and L.-L. Wang, "Magnetic properties in BiFeO3 doped with Cu and Zn first-principles investigation," *Journal of Alloys and Compounds,* 674 463-69 (2016).
105. H. Singh and K. L. Yadav, "Structural, dielectric, vibrational and magnetic properties of Sm doped BiFeO3 multiferroic ceramics prepared by a rapid liquid phase sintering method," *Ceramics International,* 41[8] 9285-95 (2015).
106. Y. Gu, J. Zhao, W. Zhang, S. Liu, S. Ge, W. Chen, and Y. Zhang, "Improved ferromagnetism and ferroelectricity of La and Co co-doped BiFeO3 ceramics with Fe vacancies," *Ceramics International,* 42[7] 8863-68 (2016).

107. Z. Zhang, H. Liu, Y. Lin, Y. Wei, C.-W. Nan, and X. Deng, "Influence of La Doping on Magnetic and Optical Properties of Bismuth Ferrite Nanofibers," *Journal of Nanomaterials,* 2012 1-5 (2012).
108. S. V. Baryshnikov, E. V. Charnaya, A. Y. Milinskii, A. A. Antonov, and A. S. Bugaev, "Phase transitions in the (BaTiO3)x/(BiFeO3)1−x composite ceramics: Dielectric studies," *Composites Part B: Engineering,* 80 15-19 (2015).
109. J. M. Liu, F. Gao, G. L. Yuan, Y. Wang, M. Zeng, and J. G. Wan, "Ferroelectric and magnetoelectric behaviors of multiferroic BiFeO3 and piezoelectric-magnetostrictive composites," *Journal of Electroceramics,* 21[1-4] 78-84 (2007).
110. H. B. Sharma, K. Nomita Devi, V. Gupta, J. H. Lee, and S. Bobby Singh, "Ac electrical conductivity and magnetic properties of BiFeO3–CoFe2O4 nanocomposites," *Journal of Alloys and Compounds,* 599[Supplement C] 32-39 (2014).
111. P. Uniyal and K. L. Yadav, "Synthesis and study of multiferroic properties of ZnFe2O4-BiFeO3 nanocomposites," *Journal of Alloys and Compounds,* 492[1-2] 406-10 (2010).
112. J. Zhu, M. Ye, and A. Han, "Preparation and microwave absorption properties of BiFeO3 and BiFeO3/PANI composites," *Journal of Materials Science: Materials in Electronics* (2017).

ACKNOWLEDGEMENT OF PREVIOUS PUBLICATIONS

1. L.A. Pérez-Maqueda, E. Gil-Gonzalez, M.A. Wassel, S.K. Jha, A. Perejón, H. Charalambous, J. Okasinksi, P.E. Sanchez-Jimenez, and T. Tsakalakos, "Insight into the BiFeO3flash sintering process by in-situ energy dispersive X-ray diffraction (ED-XRD)," Ceramics International, accepted May 2018.
2. M.A. Wassel, L.A. Pérez-Maqueda, E. Gil-Gonzalez, H. Charalambous, A. Perejón, S.K. Jha, J. Okasinksi, and T. Tsakalakos, “Flash sintering of $BiFeO_3$ at 500°C by in-situ energy-dispersive X-ray diffraction.” In preparation.